공학박사학위논문

액상 중합체 및 금속염을 활용한 변형 센서의 제작 및 응용

Fabrication of a Liquid Polymer/Metallic Salt-Based Strain Sensor and its Applications

2022년 8월

서울대학교 대학원

기계항공공학부

이 현 재

액상 중합체 및 금속염을 활용한 변형 센서의 제작 및 응용

Fabrication of a Liquid Polymer/Metallic Salt-Based Strain Sensor and its Applications

지도교수 이 정 훈

이 논문을 공학박사 학위논문으로 제출함

2022년 4월

서울대학교 대학원

기계항공공학부

이 현 재

이현재의 공학박사 학위논문을 인준함

2022년 6월

위 원 장 : 최 만 수 (인)

부위원장 : 이 정 훈 (인)

위 원 : 고 승 환 (인)

위 원 : 한 경 원 (인)

위 원 : 정 한 영 (인)

Abstract

Fabrication of a Liquid Polymer/Metallic Salt-Based Strain Sensor and its Applications

Hyun Jae Lee
Department of Mechanical and Aerospace Engineering
Seoul National University

A variety of stretchable strain sensors have been developed for various applications in diverse fields. Based on their core function represented by the conversion of mechanical deformations into electrical signals, numerous fabrication techniques combined with miscellaneous combinations of materials have been suggested and applied for different purposes. Recently, a series of innovations in agriculture in the name of smart farming have been achieved to meet increasing needs for high-quality crops. As part of the collection of essential information for plant growth, it becomes indispensable to measure axial dimensions of trees or fruits. Although certain kinds of apparatuses were reported to show precise size measurement for the trunk of a tree or the diameter of a fruit, improved instruments categorized as dendrometers had been awaited to overcome current limitations such as bulkiness, complexities in working mechanisms, dependence on users, expensiveness, etc.

In this study, I proposed a liquid polymer/metallic salt-based stretchable strain sensor. Compared to conventional strain sensors often used as wearable sensors for instant motion detection, the newly developed sensor included conductive liquid

made of silver nitrate and polyethylene glycol (PEG). The introduction of this liquid polymer brought high viscosity and chemical stability while the addition of silver nitrate supplied electrolytes in the conductive liquid. The formation of the structure of the stretchable strain sensor was finalized with a mixture of distinct elastomers called polydimethylsiloxane (PDMS) and Ecoflex. After multiple experiments, the optimal mixing ratio (20:80) of these elastomers was found to reach the equilibrium between strain, stress and stickiness, which was essential to the effective monitoring of fruit growth. The performance of the stretchable strain sensor was analyzed, showing highly linear relationships between strain and resistance as well as good repeatability. The fruit monitoring test demonstrated the stability of the stretchable strain sensor at least for two weeks with increasing ratios of 1.7 to 3.9 kΩ/mm. As an alternative instrument for fruit growth measurement, this tunable band-shaped sensor would be able to show industrial potential in terms of simple fabrication, reliable measurement, and long-term evaluation.

The use of the composite of silver nitrate and PEG also led to the development of an antenna-shaped biomimetic tactile sensor. The conductive liquid was selected to imitate the aqueous cavity of the hair of insects while wires connecting the conductive liquid and the measurement system of the sensor were installed to realize the tubular body, whose role is to transmit mechanical deformation-driven electric signals to the central nervous system of insects. This bio-inspired tactile sensor was designed to compensate the malfunction of visual sensors exposed to dark areas. The performance test of the tactile sensor through wall scanning experiments proved its ability to detect various geographical features expressed on three dimensional (3D)-printed walls with repeatable and linear relationships between bending angle and resistance. The working mechanism established with

the conductive liquid and wires revealed that the resistance of the tactile sensor would be decided by the positioning of wires in the composite of silver nitrate and PEG. When the distance between a wall and the tactile sensor was fixed during the scanning, the bio-inspired tactile sensor could offer reliable resistance data enough to reconstruct surrounding geographical features with high accuracy. This antenna-shaped biomimetic tactile sensor was characterized by the use of novel materials compared to existing tactile sensors, the adoption of a simple fabrication process, the investigation of an alternative working mechanism, the establishment of high repeatability based on bending angle and resistance, and the presentation of a perspective of being studied further for 3D image reconstruction.

Keywords : liquid polymer, polyethylene glycol, silver nitrate, dendrometer, fruit growth, tactile sensor,
Student Number : 2015-30163

Table of Contents

List of Figures

List of Tables

Chapter 1. Introduction

1.1 Conventional strain sensors

The purpose of strain sensors is to convert mechanical deformations such as elongation and compression into electrical signals. Previously, fabrication methods in combination with microelectromechanical systems (MEMS) were often used to realize strain sensors with high accuracy. Recently, the use of numerous conductive nanomaterials and elastomers have enabled researchers to develop highly deformable and sensitive strain sensors without depending on clean room process known for its complexity [1-4]. However, most of these sensors were made with solid materials, which would limit their stretchability due to fixed intermolecular distances. Moreover, the irreversibility of cracks created during stretching or bending could hinder the long-time continuous use of these sensors.

As an alternative method to minimize the limitations of solid materials, strain sensors consisting of liquid materials have been suggested. Liquid materials can include liquid metals, ionic liquids, and liquid/conductive nanoparticles composites [5-10]. Given that the majority of these sensors were aimed at the measurement of immediate mechanical responses, research on the long-term reliability of strain sensors has not been reported enough to prove the potential to be applied for long-term evaluation. For this purpose, strain sensors using liquid materials would need to assure their thorough sealing process as well as their mechanical, electrical and chemical stability. In addition, it is crucial to find appropriate fabrication techniques based on the compatibility of chemical substances, which would be able to enhance the reproducibility of targeted strain sensors. It has to be noted that in case of using conductive nanoparticles with liquid materials, their molecular

behavior might be different from when spread in solid materials because the role of ions in liquid materials is supposed to be dominant in the generation of electric current [11]. For this reason, the creation of a liquid composite for conductive liquid-based strain sensors requires the consideration of chemical relationships between each element.

1.2 Strain sensors in agricultural engineering

The transition from traditional agriculture to smart farming necessitates a sophisticated controlling system of cultivation. The attainment of this system demands various sorts of sensors, one of which would be a sensor for the measurement of plant growth [12]. The intensive monitoring of dimensional increments of fruits can help farmers optimize environmental parameters such as light, temperature and irrigation. In agriculture, dendrometers with several working mechanisms were developed to measure the volumetric expansion of trees or fruits [13-16]. For example, an optoelectronic dendrometer collects information about the infrared light reflected from a plant to convert it into voltage [13]. Although this dendrometer shows high resolution, its bulkiness and limited measurable range would not be suitable as a portable apparatus. An optical dendrometer made with an optical fiber measures the optical loss of transmission light caused by the axial growth of a tree [14]. However, the metallic body which covers the optical fiber could restrain the natural growth of a tree due to its small flexibility. On the other hand, dendrometers inspired by strain gauges are portable, easy to install, and cost-effective when compared to MEMS-based ones. The disadvantage of these sensors is that they are not well adjustable for plants of different species because of the use

of metallic materials. Therefore, it was necessary to develop alternative dendrometers with a wide range of measurement, easy adjustment, and a simple fabrication process. The application of conductive liquid-based strain sensors in agriculture would be able to give an excellent answer to the current issues related to the measurement of plant growth.

1.3 Current tactile sensors

The elaboration of artificial tactile sensing systems has been sought by a lot of researchers. Especially, the antenna of insects or the whisker of animals has been imitated using diverse materials and fabrication methods [17-21]. As a mechanoreceptor, insects mainly rely on the antenna to recognize obstacles, avoid collisions, and detect air vibrations [22-25]. Several types of tactile sensors inspired by the antenna of insects have been reported [22,26-29]. As an example, a bionic feller using damped harmonic oscillations was reported to calculate the distance with an unknown object, and to identify the general properties of materials based on the frequency of oscillations [22]. A MEMS tactile sensor was composed of two angle detectors and one contactor to conduct the angle correction when detecting objects [26]. A cilia tactile sensor was designed mainly with iron nanowires, PDMS, and a magneto-impedance sensor to calculate changes in magnetic field in case of the deflection of the sensor [27]. A wind sensor was developed with silver nanoparticles and polyethylene terephthalate (PET) to detect air flow using magnetic field [28]. A morphological study on the mechanoreceptor of insects was reported to understand its composition and sensing mechanism before fabrication [29]. However, each of the aforementioned sensors is fragile,

hard to miniaturize, and can easily be affected by environmental factors. Moreover, the anatomical features of insect mechanoreceptors were not minutely considered as key elements to elaborate biomimetic tactile sensors. For these reasons, a new type of bio-inspired tactile sensor would be required for military purposes.

1.4 Tactile sensors in military industries

The artificial tactile sensing system inspired by the antenna of insects can be used to understand geometric background in unknown areas where optical sensors are not capable of showing proper performance. In modern warfare, the importance of biomimetic robots is increasing due to its efficiency in obtaining information about uncharted surroundings as well as its role to save the lives of soldiers. In this sense, biomimetic robots containing tactile sensors would be able to offer useful information to soldiers to protect themselves against unpredictable situations. However, few tactile sensors are suitable for military operations because of their bulkiness, fragility, and difficulty in cost-effective mass production. A miniaturized size can provide a biomimetic tactile sensor with camouflage from enemies. The use of sturdy and elastic materials is expected to maintain high and long-term durability in harsh environment. In comparison with MEMS-dependent fabrication, a simplified fabrication process established out of a clean room would be able to facilitate rapid field applications. The biocompatibility of materials utilized for a biomimetic tactile sensor can be an advantage for military industries.

1.5 Research objectives and contributions

The liquid polymer/metallic salt-based stretchable strain sensor was developed to show the use of a new composite for a liquid-based stretchable strain sensor. Although numerous kinds of liquid metals, ionic liquids, and liquid/conductive nanoparticles composites were previously tested by other researchers, the application of a composite of PEG and silver nitrate would be the first case as a stretchable strain sensor. An appropriate combination of liquid polymer and metallic salt can enhance chemical stability and electrical conductivity at the same time. Secondly, this stretchable strain sensor led to the establishment of a novel fabrication technique after its profound analysis especially regarding the interface between the liquid composite and the mixture of elastomers during the hardening process. For liquid-based strain sensors, the selection of a proper sealing process is essential to guarantee their quality. Compared to conventional sealing processes such as layer bonding and liquid injection with a syringe, I proposed an alternative sealing process based on the chemical relationship and compatibility of the liquid composite and the mixture of elastomers. Thirdly, the mechanical properties of the newly developed stretchable strain sensor were carefully taken into account to achieve the optimal condition as a stretchable strain sensor for the effective monitoring of fruit growth. The use of two distinct elastomers enabled me to discover an ideal mixing ratio to satisfy large strain, low stress, and less stickiness, which would be indispensable for the measurement of fruit growth. Fourthly, a stretchable strain sensor aimed at long-term and reliable measurement was realized with the confirmation of its performance with fruit samples. The two-week intensive monitoring of fruit growth proved that this stretchable strain sensor

would have the possibility to be applied for long-time evaluation.

The antenna-shaped tactile sensor based on conductive liquid and elastomers was invented to suggest an alternative bio-inspired tactile sensor with a realistic figuration of the antenna of insects. Particularly, the sensillum of insects mainly consisting of a seta, lymph space, and a tubular body is the core unit of the tactile sensing system [30], which was realized with a mixture of elastomers, a composite of PEG and silver nitrate, metallic wires. Secondly, the adoption of this liquid composite for a tactile sensor would be the first to be reported while a strain sensor with this liquid composite was recently shown [31]. Usually, the utilization of liquid material allows larger deformations compared to solid materials [7]. The composite of PEG and silver nitrate is known for a useful method to form silver nanoparticles, and for its long-term chemical stability up to several months [32,33]. Thirdly, the involvement of a 3D printer in the fabrication process resulted in cost-effective and rapid fabrication. The 3D printer facilitates the adjustment of the size and shape of a tactile sensor for its integration into a biomimetic robot. Fourthly, a geographical reconstruction test with multiple tactile sensors opened up a route towards 3D image reconstruction. Repeated scanning experiments with 3D printed wall enabled me to find out a novel method of calculation for geographical reconstruction using a relationship between the bending angle and the resistance.

In summary, the two different sensors that I created demonstrated a perspective of new chemical elements, simple but sophisticated fabrication, alternative working principle, and long-term reliability. I believe that these liquid polymer/metallic salt-based sensors would be able to contribute to the significant development of smart farming and military industries.

Chapter 2. Fabrication of a stretchable strain sensor

I present an indigenous liquid polymer/metallic salt-based stretchable and transparent strain sensor for the measurement of axial dimensions of fruits and stems as shown in Figure 2-1.

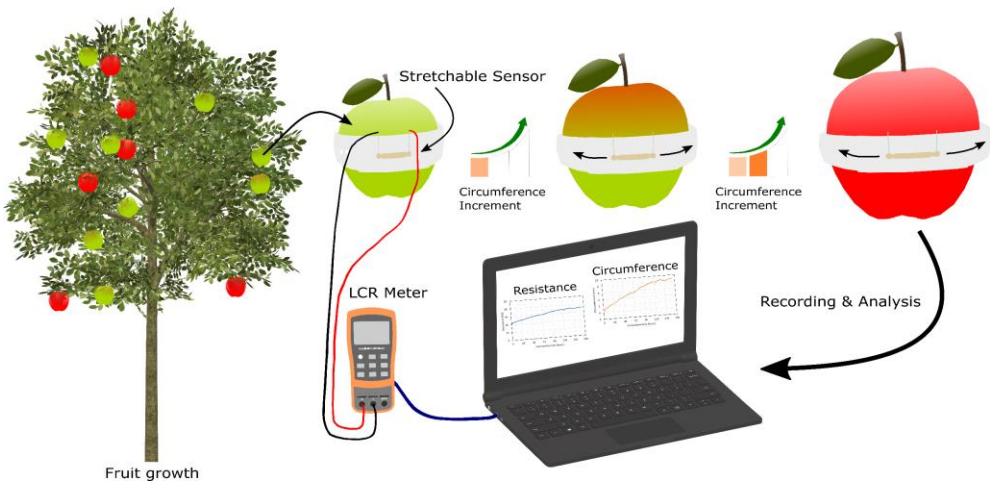

Figure 2-1. Schematic illustration of the use of a stretchable sensor for fruit growth measurement.

2.1 Synthesis of polyethylene glycol (PEG)/silver nitrate composites

A combination of 2 mL of PEG 200 (Sigma-Aldrich) and 1 g of silver nitrate (Samchun chemicals) was manually mixed and stirred for 20 minutes in a Petri dish at room temperature. Likewise, the same combination was reproduced in two more Petri dishes. Once the silver nitrate was completely dissolved in PEG, two of the Petri dishes were kept in a convection oven (Sanyo) at 70°C, one of which for 2 hours and the other for 4 hours. The third mixture was stored at room temperature without heating. The samples were taken out from the oven after 2 and 4 hours,

cooled down, and carefully shifted into microcentrifuge tubes. These three liquid combinations would necessarily make the sensor part and were studied independently when incorporated inside the flexible band.

2.2 Fabrication of a strain sensor with the liquid composites

A mold with dimensions of 40 mm × 20 mm × 3 mm for the sensor structure was designed using AutoCAD 2020 and the same was printed with a 3D printer (DP200, Sindoh). Polydimethylsiloxane (PDMS, Sylgard 184, Dow Corning) and Ecoflex (00-30, Smooth-on) were mixed at a ratio of 40:60 in a conical tube at room temperature. Centrifugation for 5 minutes at 25℃ with a centrifuge (Combi-514R, Hanil science industrial) was necessary at this juncture to remove redundant gas trapped in the blend. This mixture of elastomers was poured into the mold and was kept at 45℃ for 4 hours in an incubator (Thermo Scientific). The cured mixture was peeled off from the mold. The entire size of the sensor structure was 36 mm × 16 mm × 1.75 mm, and its channel size was designed to be 19 mm × 3 mm × 0.5 mm. Nichrome wires of 250 μm diameter were inserted through the sidewalls of the structure until the wires reached the channel. The sensor structure was treated for 25 seconds in a plasma chamber (Femto Science) to make the surface of the channel hydrophilic. The composite of PEG and silver nitrate (55 μL) was poured into the channel and placed in a vacuum desiccator (Lab Companion) for 1 hour to remove the gas bubbles. Then, the same mixture of elastomers was carefully poured onto the surface of the liquid-filled channel until the upper part of the structure is completely covered. After being kept at room temperature for 2 hours,

the entire structure was cured at 45℃ for 4 hours in the incubator, thus completing the first phase of the fabrication process.

2.3 Preparation of a flexible band for the incorporation of the strain sensor

A preform for the flexible band was designed with AutoCAD 2020 and printed using the 3D printer (DP200, Sindoh) with dimensions of 250 mm × 30 mm × 6 mm. For the mixture of elastomers, PDMS (Sylgard 184, Dow Corning) and Ecoflex (00-30, Smooth-on) were mixed at a ratio of 20:80 in a conical tube at room temperature. After the centrifugation for 5 minutes at 25℃ with a centrifuge (Combi-514R, Hanil science industrial) to remove undesirable gas bubbles, this mixture of elastomers was poured into the preform and cured at 45℃ for 4 hours in the incubator (Thermo Scientific). Taken out from the incubator, the preform was cooled down and the cured mixture of elastomers was carefully peeled off from the preform.

2.4 Encapsulation of the strain sensor into the flexible band

Both the stretchable strain sensor and the flexible band were analyzed for any unexpected damages which could have happened during the fabrication process. The strain stretchable sensor was placed into the flexible band, completely encapsulated by the mixture of PDMS and Ecoflex at a ratio of 20:80, and cured at 45℃ for 4 hours in the incubator.

Chapter 3. Methods for the stretchable strain sensor

3.1 Measurement of strain and resistance

The aim of this experiment was to measure and record the strain-induced electrical resistance. For this purpose, a syringe pump (Legato 110, KdScientific) was employed to precisely stretch and release the flexible band at fixed velocities for a fixed length. Different sensor samples, filled with the liquid composites treated at different temperatures (Non-heated, 70℃ for 2 hours, and 70℃ for 4 hours), were tested under stretching and releasing rates of 20 μm/s, 100 μm/s, and 200 μm/s for 6 cm respectively. Resistance changes were measured and recorded using a digital LCR meter (U1733C, Keysight) with an interval of one second at 1 kHz.

3.2 Tensile strength measurement

Distinct band samples having the similar dimensions (250 mm × 30 mm × 6 mm) were tested under a universal testing machine (UTM, Instron-5543). Each sample was made using different mixing ratios of PDMS and Ecoflex (PDMS 100%, PDMS 80% - Ecoflex 20%, PDMS 60% - Ecoflex 40%, PDMS 40% - Ecoflex 60%, PDMS 20% - Ecoflex 80%, Ecoflex 100%). Especially, one sample was prepared with the mixing ratios of PDMS 20% - Ecoflex 80% for the flexible band and of PDMS 40% - Ecoflex 60% for the sensor part where the stretchable strain sensor is embedded. The load applied by the UTM was 1 kN and the pulling speed was 5 cm/min.

3.3 Ultraviolet-visible (UV-Vis) spectroscopy

Differently treated liquid composites were used to verify the presence of reduced silver nanoparticles with a UV-Vis spectrometer (V-770, JASCO). The liquid composites tested for the absorbance of light of silver nanoparticles were made and treated at various temperatures (Non-heated, 70℃ for 2 hours, and 70℃ for 4 hours).

3.4 Field emission-scanning electron microcopy (FE-SEM) and elemental analysis

PEG- silver nitrate solution was centrifuged at an RPM of 15,900 for 50 minutes. After removing PEG from the top, the sediment particles were washed with 100% ethanol for three times, and dried in a convection oven at 70˚C for 4 hours. The morphology of silver particles was analyzed through FE-SEM (JSM-7800F Prime, JEOL Ltd, Japan), and its presence was analyzed through EDS (X-Max^N, OXFORD INSTRUMENTS).

3.5 Fruit model simulation

Oval fruit models with diameters of 6.5 cm, 7.5 cm, and 8.5 cm were prepared using the 3D printer for the fruit model simulation. The idea behind this experiment was to observe the stability of the flexible band in terms of changes in resistance for a longer time duration. The circumferences of the fruit models were covered with different sensor bands made at the aforementioned conditions (Non-heated, 70℃ for 2 hours, and 70℃ for 4 hours). Resistance changes were registered using

the digital LCR meter at an interval of every second for one hour for each measurement.

3.6 Performance test as a dendrometer using real fruits

One fruit from a mandarin tree and the other from a passion fruit tree were selected for the performance test as a dendrometer for fruit growth measurement. The temperature and the humidity were maintained between 24-26℃ and between 25-35% respectively. Resistance changes were recorded using the two digital LCR meters with an interval of 30 seconds for two weeks. Nichrome wires of a diameter of 250 μm were used to measure approximate circumference changes.

Chapter 4. Analysis of the stretchable strain sensor

4.1 Formation of PEG/silver nitrate composites

The fabrication process of the polymer metallic salt-based stretchable strain sensor is briefly shown in Figure 4-1. After separating the sensor structure and the band structure from the molds (Figure 4-1a), the composite of PEG and silver nitrate was encapsulated into the sensor structure to make the stretchable sensor (Figure 4-1b). Then, the stretchable sensor was incorporated into the band structure to realize the entire stretchable strain sensor with the flexible band (Figure 4-1c). Figure 4-1d represents the final product.

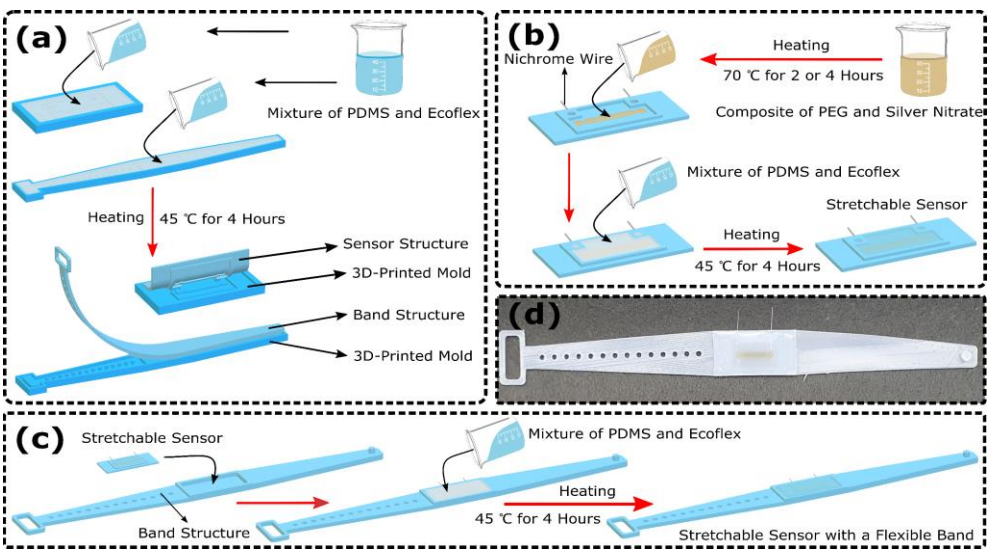

Figure 4-1. Fabrication process of the polymer/metallic salt-based stretchable strain sensor. a) Preparation of a sensor structure and a band structure using a mixture of PDMS and Ecoflex. b) Synthesis of liquid composites at different heating temperatures and the preparation of the stretchable sensor. c) Fabrication of the entire stretchable sensor with a flexible band. d) Photograph of the final product.

PEG in the formation of the composite of PEG and silver nitrate provides the chemical stability of the liquid composite. PEG is also known as a reducing agent for the formation of silver nanoparticles [34,35]. Silver has a low tendency of ionization compared to other metals. In other words, silver ions have strong oxidizing power in order to be reduced to metallic silver. After the chemical reaction between PEG and silver nitrate, the silver ions are thought to be detached from silver nitrate and get reduced while the functional group of PEG is transformed from the hydroxyl group to the aldehyde group [32,33,36]. Given that substances with both these functional groups are polar but do not usually ionize, good conductivity confirmed from the following characteristic tests of the stretchable strain sensor might be related to the formation of separate electrolytes in the composite of PEG and silver nitrate. It is believed that the electrolytes present in the liquid composite are hydrogen ions and probably nitrate ions [32,36]. Even though PEG has weak polarity and dissolves a less amount of inorganic or metallic salts compared to water, the oxidation-reduction reaction between silver ions and the end group of PEG leads to the supply and dispersion of these additional electrolytes. The probable composition of the liquid composite after the chemical reactions is shown in Figure 4-2a. It was also reported that the combination of PEG and silver nitrate was stable for months in terms of chemical properties, which proves that this liquid composite could be a useful combination for long-term measurement [32,33]. Resistance changes caused by stretching and releasing can be calculated using the equation mentioned below.

$$R = \rho \frac{L+\Delta L}{(W+\Delta W)(H+\Delta H)} \quad (1)$$

where R is the resistance, ρ is the resistivity, and L, H, W are the length, the width and the height respectively. One thing that is different from solid-state strain sensors is that the total volume of the channel of the sensor will not be changed after stretching because liquids are not compressible [37]. The composition of the liquid polymer and the electrolytes used in our research is also different from polyelectrolytes whose repeating units have an electrolyte group [38,39].

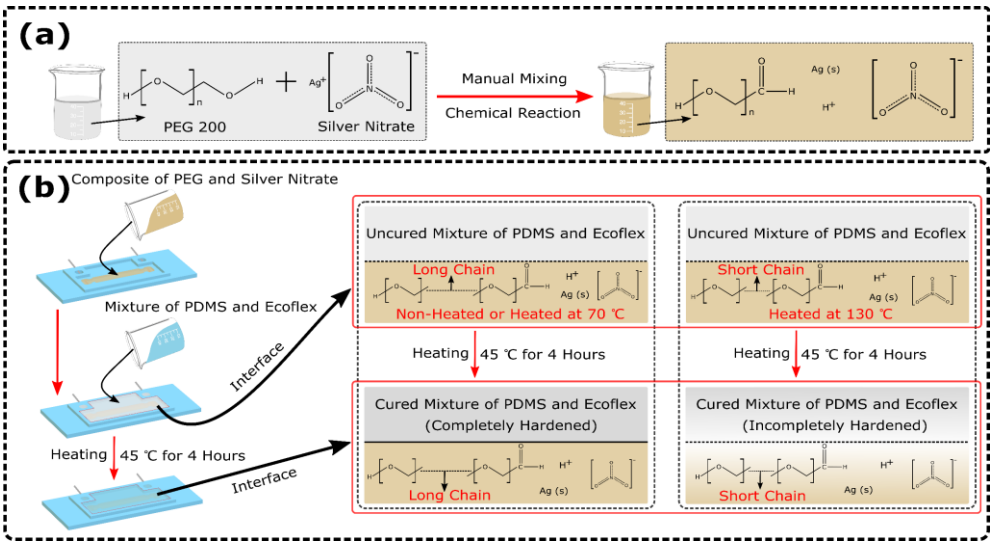

Figure 4-2. Schematic illustrations of the chemical reactions in the composite of PEG and silver nitrate and in its interface with the mixture of PDMS and Ecoflex. a) Before and after the chemical reactions of the liquid composite. b) Chemical reactions in the interface between the mixture of the elastomers and the liquid composites treated at different heating temperatures.

4.2 Sealing process of the strain sensor

When it comes to the sealing of liquid-state strain sensors, several liquid encapsulation methods have been presented such as the bonding of two layers, the injection of liquids into the channel, and the covering with uncured elastomers [10, 40-43]. The bonding of two layers often using plasma treatment or other similar

techniques cannot completely fuse two layers. The injection of liquids into the channel makes tiny holes which might cause an unexpected leakage of liquids. The removal of the air when filling out the channel is challenging as well. Our encapsulation method is composed of the effective sealing of the sensor mainly based on the polarity and chemical reactivity of each element. The composite of PEG and silver nitrate has some polarity because of its carbon-oxygen double bonds formed after the reaction between PEG and silver nitrate while the mixture of PDMS and Ecoflex has very less polarity [44-47]. It was reported that silicone elastomers such as PDMS and Ecoflex are cured through the platinum-catalyzed hydrosilylation [48,49]. During the curing process, hydrogen-siloxanes present in the curing agent react with the vinyl group of siloxane oligomers to form an elastic network with carbon-silicon bonds [50]. The composite of PEG and silver nitrate contains long molecular chains with strong covalent bonds, which might enable it to stay intact and to be less reactive with the uncured mixture of elastomers (Figure 4-2b). On the other hand, it was also reported that if PEG is heated at more than 70℃, it undergoes thermal oxidative degradation [51]. Thermal oxidative degradation includes structural defects, second cross-linking or disruptions in molecular chains, which can create byproducts such as ethylene glycol and PEG of lower molecular weights [51]. Especially, when we made samples with the liquid composite treated at 130℃, the uncured mixture of elastomers was not completely hardened as shown in Figure 4-2b. Therefore, it is supposed that a probable increase of the reactivity of this composite caused by the thermal oxidative degradation of PEG facilitates the interaction with the uncured elastomers in the curing process, which results in an incomplete hardening of the cover of the sensor. Between each elastomer, the uncured mixture of elastomers was proven to be well

mixed without any incomplete curing after the curing process. It is thought that the compatibility of these two elastomers is due to their common curing process including the platinum catalyst. Regarding the connection between liquids and outer electronic components, silver paste was used in some other papers [4,5,9]. However, when silver paste hardens, it becomes rigid and fragile to external deformation. In our sensor, a simple vertical insertion of thin metal wires through the structure allowed us to eliminate silver paste from the scenario and to effectively fix electric wires which can be connected to the measurement system.

4.3 Correlation between strain and resistance

For each experiment, 3 sensor samples with differently treated liquid composites (Non-heated, 70℃ for 2 hours, and 70℃ for 4 hours) were stretched and released for 3 times and mean values were calculated (Figure 4-3a). Samples with the non-heated liquid composites showed resistance changes (ΔR) of 18.5% with respect to its initial resistance value (R_0) for the stretching of 6 cm (Figure 4-3b-i) while those with the liquid composite treated at 70℃ for 2 and 4 hours showed 16.3% and 16.0% respectively (Figure 4-3c-i, Figure 4-3d-i). The maximum standard deviations were 3.1 % for the samples with non-heated liquid composite, 0.9% for the samples with the liquid composite treated at 70℃ for 2 hours, and 2.1 % for the samples with the liquid composite treated at 70℃ for 4 hours. This result states that in general, heated samples were chemically stable compared to the non-heated samples and that specifically the liquid composite treated at 70℃ for 2 hours outperformed other samples in chemical stability with the smallest standard deviation. Regarding the liquid composite treated at 70℃ for 4 hours, although the

difference in absolute resistance values between each sample was greater than that of the liquid composite treated at 70℃ for 2 hours, each sample showed more repeatable results with less mean standard deviations. Every graph of the time-resistance relationship represents high coefficients of determination ($R^2 > 0.99$), which means that resistance changes caused by stretching and releasing at a regular speed follow highly linear trend lines. These linear changes were also confirmed in the graphs showing strain-resistance relationships (Figure 4-3b-ii, Figure 4-3c-ii, Figure 4-3d-ii). The gauge factors were calculated with respect to strains as well (Figure 4-3b-iii, Figure 4-3c-iii, Figure 4-3d-iii). All the graphs show gauge factors of 0.5 to 0.7 until the strain of 30% and Figure 4-3c-iii shows the narrowest range of standard deviation (0.03~0.09). Among the 3 types of samples, the samples with the liquid composite treated at 70℃ for 2 hours have more stability than the other types of samples in terms of resistance changes and the gauge factor. Nevertheless, resistance variation ratios ($\Delta R/R_0$) of these 3 different types of samples did not show significant difference, which suggests that the difference in the size and shape of silver nanoparticles in the composites does not affect the electrical resistance in a meaningful way. The formation of silver nanoparticles based on the temperature and the time of heating will be described in the following section.

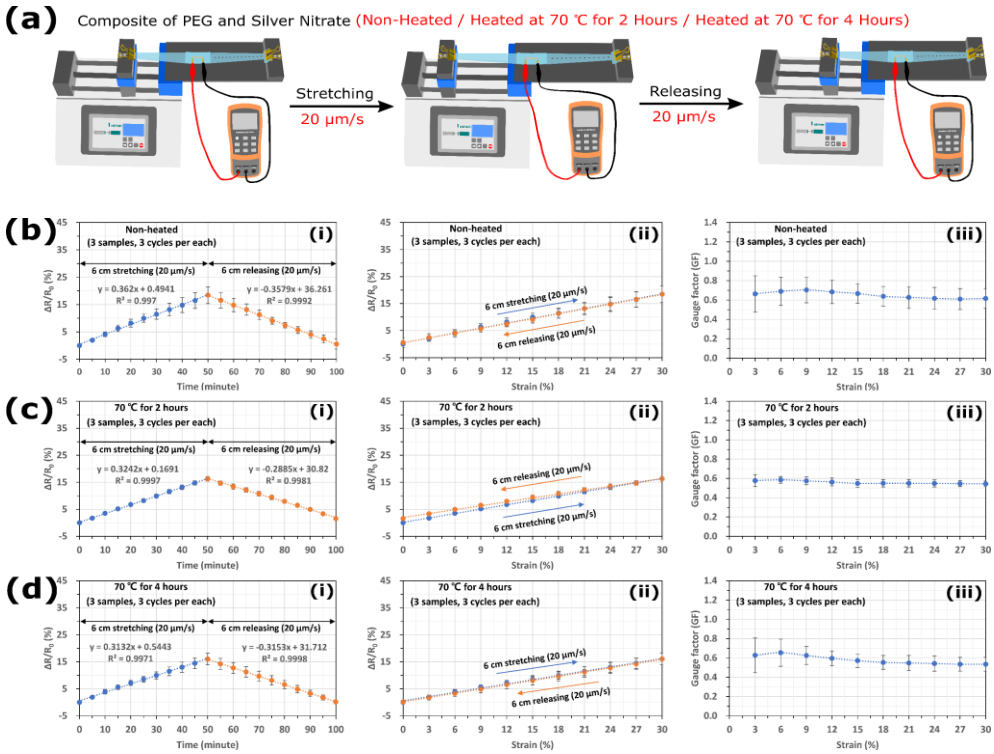

Figure 4-3. Measurement of the relationship between strain and resistance. a) Schematic illustration of the measurement system and the experiment conditions. b) Samples with the non-heated liquid composite, (i) Time & resistance changes, (ii) Strain & resistance changes, (iii) Strain & gauge factor. c) Samples with the liquid composite treated at 70℃ for 2 hours, (i) Time & resistance changes, (ii) Strain & resistance changes, (iii) Strain & gauge factor. d) Samples with the liquid composite treated at 70℃ for 4 hours, (i) Time & resistance changes, (ii) Strain & resistance changes, (iii) Strain & gauge factor.

In another experiment, as shown in Figure 4-4a, the 3 types of samples mentioned above were stretched and released for 3 cycles at 3 different velocities and mean values were presented on the graphs. In Figure. 4-4b-i, Figure 4-4c-i, and Figure 4-4d-i, it was found that the slope of resistance changes is the highest in the sample with the non-heated liquid composite. The same experiments were conducted at 100 μm/s (Figure 4-4b-ii, Figure 4-4c-ii, Figure 4-4d-ii) and 200 μm/s

(Figure 4-4b-iii, Figure 4-4c-iii, Figure 4-4d-iii) respectively. Regardless of velocities, every sample showed high repeatability and linear resistance changes with high coefficients of determination. The difference in absolute resistance values between the 3 types of samples might be due to minute irregularities of the amount of the composites poured into the channels.

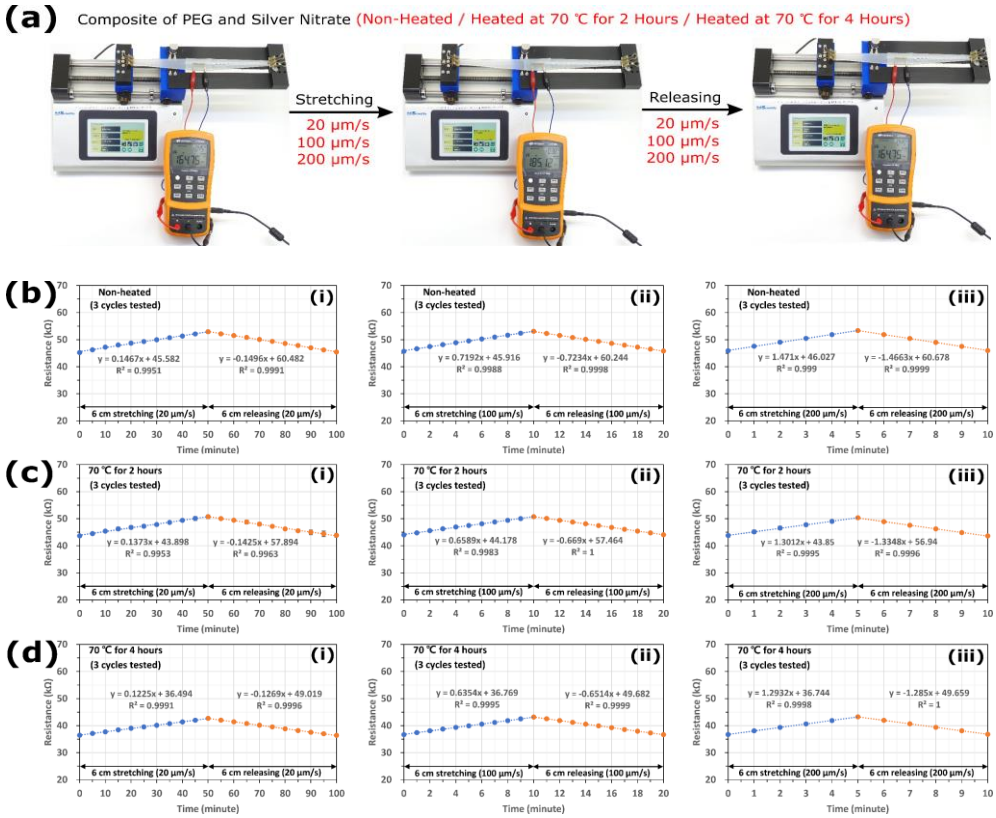

Figure 4-4. Measurement of the relationship between stretching velocities and resistance changes. a) Schematic illustration of the measurement system and the experiment conditions. b) Samples with the non-heated liquid composite with a stretching and releasing rate of, (i) 20 μm/s, (ii) 100 μm/s, (iii) 200 μm/s. c) Samples with the liquid composite treated at 70℃ for 2 hours with a stretching and releasing rate of, (i) 20 μm/s, (ii) 100 μm/s, (iii) 200 μm/s. d) Samples with the liquid composite treated at 70℃ for 4 hours with a stretching and releasing rate of, (i) 20 μm/s, (ii) 100 μm/s, (iii) 200 μm/s.

4.4 Comparison between theoretical calculations and experiments

The gauge factors of the sensor samples with differently treated liquid composites were shown in Figure 4-3b-iii, Figure 4-3c-iii, and Figure 4-3d-iii. If we already know the elastic modulus and the geometric information about the sensor and its fluidic channel, the resistance and the gauge factor can be predicted. From the equation mentioned in Figure 4-5, the resistivities were calculated using the initial resistance values of each sample before stretching, which were 4.75 Ωm for the samples with the non-heated liquid composite, 5.09 Ωm for the samples with the liquid composite treated at 70℃ for 2 hours, and 4.93 Ωm for the samples with the liquid composite treated at 70℃ for 4 hours respectively.

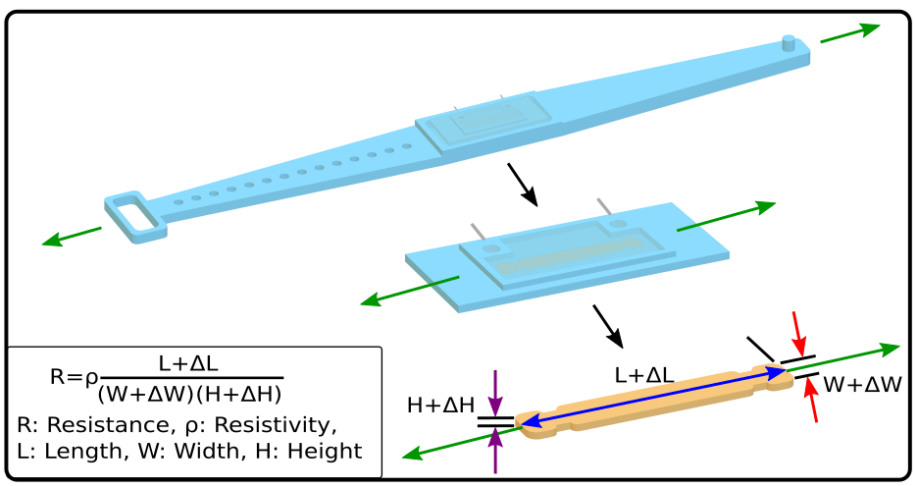

Figure 4-5. Working mechanism of resistance changes.

If we use the incompressibility of the liquid channel, the resistance after stretching can follow the equation mentioned below.

$$R = \rho \frac{(L+\Delta L)^2}{AL} \quad (2)$$

where R is the resistance, ρ is the resistivity, and A, L are the initial cross-sectional area, the initial length respectively. The length of the middle part where the sensor is located was 36 mm and that of the band structure was 82 mm for the left and right sides respectively. The young's moduli of the middle part and the band structure were estimated to be 78 kPa and 44 kPa respectively. Once the flexible band is stretched, the applied force between the middle part and the band structure has to be the same. Given that the cross-sectional area of the middle part was 82 mm^2 and that of the band structure was 51.3 mm^2, the relationship between the stresses of the middle part and the band structure can be described as below.

$$\sigma_2 = 0.625\sigma_1 \tag{3}$$

where σ_1 and σ_2 are the stress of the band structure and that of the middle part respectively. Then, the stretched length of the liquid channel and its resistance can be theoretically obtained. From the equation (3), the relationship between the strains can be also induced.

$$\epsilon_1 = 2.84\epsilon_2 \tag{4}$$

where ε_1 and ε_2 are the strain of the band structure and that of the middle part respectively. Then, the stretched length of the liquid channel and its resistance can be theoretically obtained. Figure 4-6 is the summary of the gauge factors resulting from both the experiments and the calculations with all types of samples. Theoretically calculated gauge factors were about 0.8, which is higher than those from the experiments (Figure 4-6a, Figure 4-6b, Figure 4-6c). It would be because some of geometric details could not be thoroughly inserted into the calculations. For example, the real band structure had a larger width (20.5 mm) around the

middle but a smaller width (10 mm) around the end. The other factor is that there were holes on the band structure, which is believed to affect the decrease of the gauge factors.

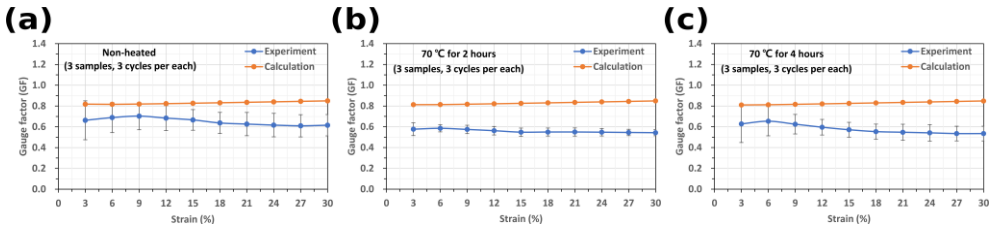

Figure 4-6. Gauge factors from calculations and experiments.

Figure 4-7 is to show the difference in resistance based on the amount of silver nitrate in PEG. The liquid composites were kept in a fixed channel. It was confirmed that there is no coherent relationship between the amount of silver nitrate in PEG and the resistance of the liquid composite. In other words, the initial resistance would be decided not simply by the amount of silver nitrate but by the chemical equilibrium of the liquid composites.

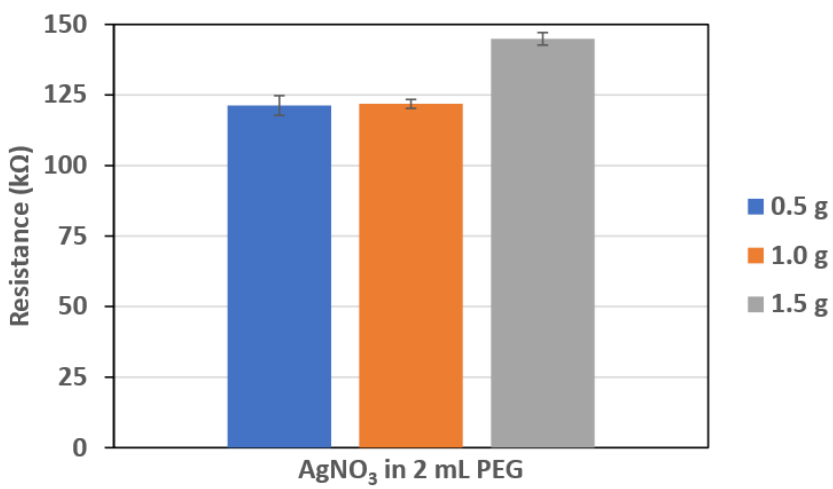

Figure 4-7. Relationship between the amount of silver nitrate in PEG and the resistance of the liquid composites.

4.5 Optimization of elasticity for large strain, low stress and high sensitivity

The elastomer samples were prepared with different mixing ratios of PDMS and Ecoflex as shown in Figure 4-8a-i. The universal testing machine (UTM) used for the tensile strength measurement is shown in Figure 4-8a-ii. Figure 4-8a-iii shows the result of tensile strength measurement. It was reported that the increasing ratio of Ecoflex in the mixture of PDMS and Ecoflex decreases the young's modulus of hybrid structures [52]. Figure 4-8a-iv presents the relationship between the PDMS / Ecoflex ratio and the elastic modulus. This graph shows that the average elastic modulus decreases from PDMS 100% to Ecoflex 100%. Given that the elastic modulus is an indication of rigidity, the sensor with smaller elastic modulus would give less pressure or stress to fruits. However, the presence of PDMS in the mixture is to reduce the stickiness of Ecoflex. If the sensor easily clings to fruit samples, it might cause an unbalanced stretching of the sensor, which can create inaccurate correlations between stretched lengths and resistance changes. Therefore, we found the optimal ratio of the two elastomers (PDMS 20% - Ecoflex 80% for the flexible band and PDMS 40% - Ecoflex 60% for the sensor part) to achieve the equilibrium between large strain, low stress and less stickiness. The ratio of PDMS 40% - Ecoflex 60% for the sensor part was synchronized with that of the sensor. This ratio was used to easily remove the sensor structure from the 3D-printed mold with the help of the increased amount of PDMS.

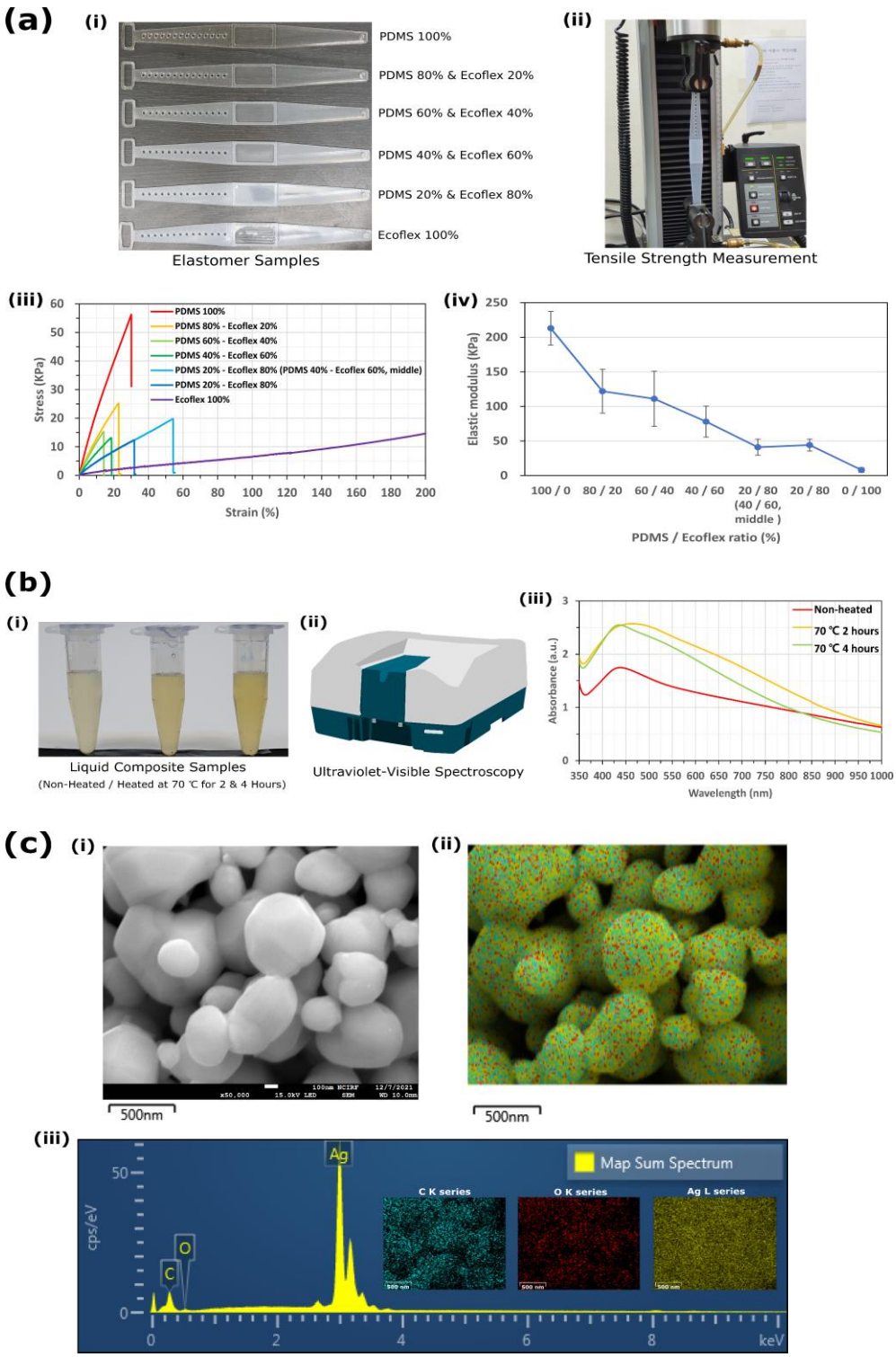

Figure 4-8. Analysis of the elastic samples and the liquid composite samples. a) Tensile strength measurement, (i) Elastomer samples with different mixing ratios of PDMS and Ecoflex, (ii) Universal testing machine, (iii) Measurement of the relationship between

strain and stress, (iv) Measurement of the relationship between PDMS / Ecoflex ratio and elastic modulus. b) UV-Vis absorption spectra measurement, (i) Liquid composite samples (non-heated, treated at 70℃ for 2 hours, treated at 70℃ for 4 hours), (ii) Ultraviolet-visible spectroscopy, (iii) Measurement of the relationship between wavelength and absorbance. c) Field emission-scanning electron microscopic (FE-SEM) image and energy dispersive X-ray spectroscopic (EDS) analysis, (i) SEM image of silver nanoparticles extracted from the composite of silver nitrate and PEG, (ii) Elemental mapping, (iii) EDS analysis of silver nanoparticles.

To assess the effect of the tensile stress of the fruit dendrometer on fruit growth, I took the thin-walled pressure vessel model. If we think about the cross-section of a cylindrical structure, it would be as shown in Figure 4-9. In this case, the circumferential stress corresponds to the stress of the sensor while the internal pressure can be considered as the pressure perceived by a fruit covered with the sensor.

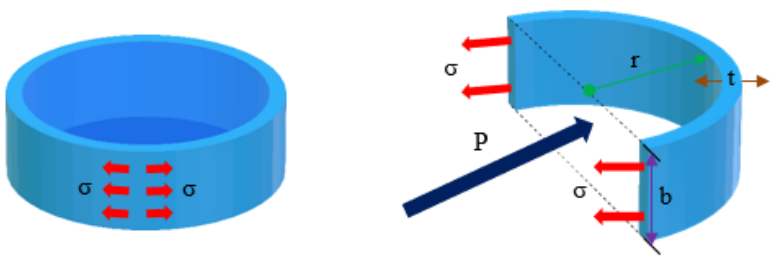

$$\sigma(2bt) = P(2rb) \Rightarrow P = \frac{t}{r}\sigma$$

σ: circumferential stress (Pa)
P: internal pressure (Pa)
b: dendrometer band width (mm)
t: dendrometer band thickness (mm)
r: fruit radius (mm)

Figure 4-9. Simulation model for the relationship between fruit growth and mechanical stress.

Based on this hypothesis, the internal pressure can be calculated using the equation in Figure 4-9. According to this calculation, the internal pressure would be proportional to the tensile stress of the sensor, which is also proportional to the strain of the sensor.

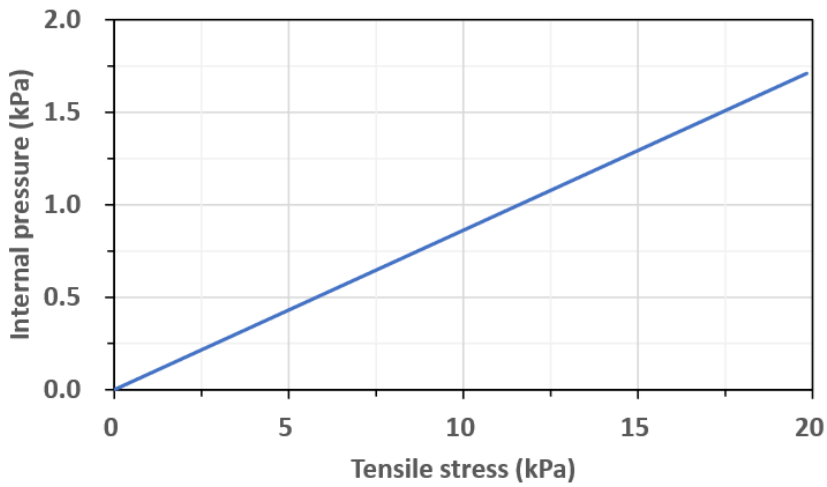

Figure 4-10. Theoretically predicted internal pressure caused by the tensile stress of the stretchable strain sensor.

4.6 Characterization of silver nanoparticles in the PEG/silver nitrate composites

The presence of silver nanoparticles in the composite of PEG and silver nitrate prove chemical reactions as expected in Figure 4-2a. Silver nanoparticles are known to absorb incident light at specific wavelengths [32,33]. The absorbance of light causes the collective oscillation of the conduction electrons on the surface of silver nanoparticles, which is called surface plasmon resonance (SPR). The SPR could be measured using ultraviolet-visible (UV-Vis) spectroscopy (Figure 4-8b-ii). It was reported that the absorbance peaks of UV-Vis spectroscopy depend on the

size and shape of particles and that silver nanoparticles with diameters of 10 to 100 nm show approximately absorbance peaks at 400 to 500 nm [53]. The graph in Figure 4-8b-iii shows the effect of the temperature and time for the treatment of the liquid composite on its intensities and absorbance peaks of light. The liquid composites treated at different temperatures or for different heating times presented gradated colors (Figure 4-8b-i) because different heating temperatures and times affect the size of silver nanoparticles [54]. It is known that silver nanoparticles in the form of colloidal silver are easily disrupted by thermal agitation, which leads to aggregation into large particles and precipitates [55]. Absorbance peaks with longer wavelengths mean bigger silver nanoparticles while higher intensities are related to silver nanoparticles with higher densities. For the confirmation of the existence of silver nanoparticles, field emission-scanning electron microscopy (FE-SEM) and energy dispersive X-ray spectroscopy (EDS) were used. Figure 4-8c-i, Figure 4-8c-ii, and Figure 4-8c-iii are the SEM image of silver nanoparticles at the magnification of 50,000×, the elemental mapping, and its EDS analysis respectively. As a result, with 95 weight percent and 70 atomic percent, we confirmed that silver nanoparticles were present in the liquid composite. Nonetheless, the role of silver nanoparticles in electric conductivity in the composite of PEG and silver nitrate might be limited [11]. In metals, free electrons are involved in electric conduction while ions play a key role in creating electric current in liquids. Therefore, although delocalized electrons are present in silver nanoparticles, electric current would be generated throughout the composite mainly by means of electrolytes. Figure 4-4 and Figure 4-8b show that no coherent relationship was found between electric conductivity and the amount or size of silver nanoparticles, which suggests that once the quantity of silver nitrate is fixed

to form the composite, electrical resistance is hardly affected by the varied formations of silver nanoparticles.

Figure 4-11 is the SEM images of silver particles made at different moments in the range of the magnification of 20,000× and 50,000×. If we focus on the composites of PEG and silver nitrate, it can be said that as time goes by, the size of silver particles increases (Figure 4-11a, Figure 4-11b, Figure 4-11c). Metallic silver was also clearly observed in the mixture of PEG and metallic silver (Figure 4-11d).

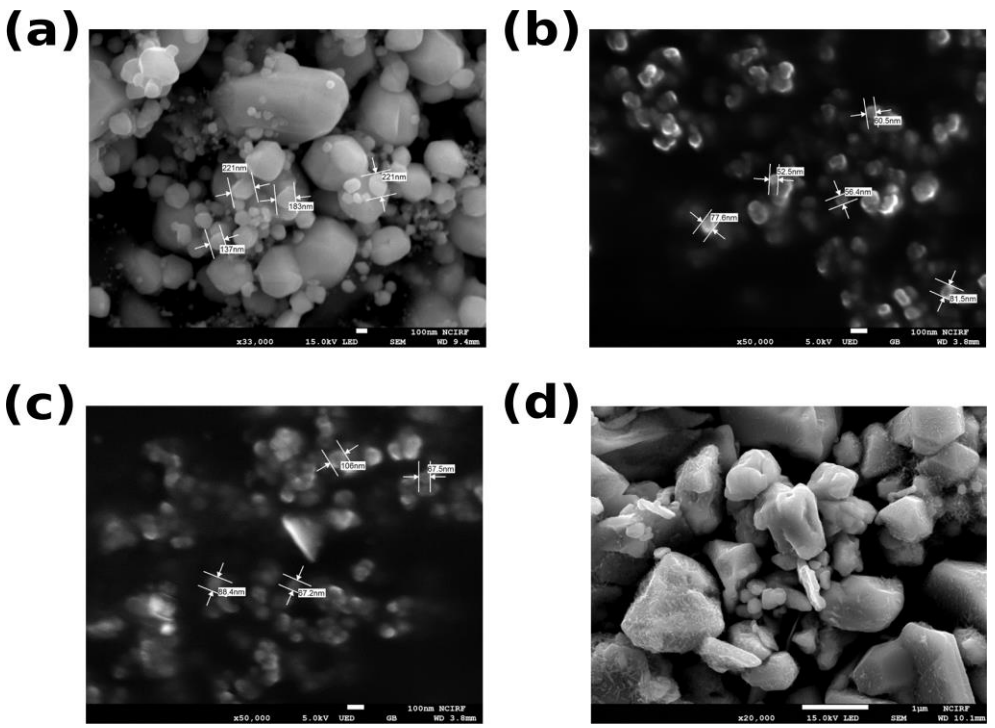

Figure 4-11. SEM images of silver particles extracted from the composite of PEG and silver nitrate and made on (a) November 19, 2021. (b) April 9, 2022. (c) May 11, 2022. (d) SEM image of silver particle extracted from the composite of PEG and metallic silver.

Figure 4-12 is the result of the investigation into the long-term effect of silver particles on the electrical conductivity of the stretchable strain sensor (Figure 4-12c,

Figure 4-12d, Figure 4-12e). The resistances of the samples made with PEG and silver nitrate at different moments are shown in Figure 4-12a. Although the size of silver particles varies in each sample, there was no remarkable difference in resistance in the liquid composites. When silver nitrate was completely removed from PEG or replaced by metallic silver, the overall resistance of the liquid channels increased. It is thought that the supply of ions from silver nitrate would significantly improve the electric conductivity of the sensor while metallic silver would also affect the reduction of the electrical resistance.

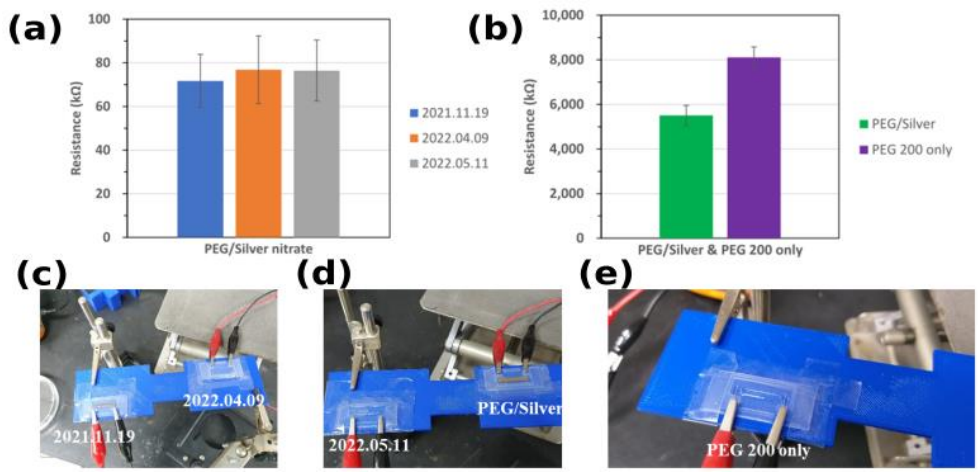

Figure 4-12. Electrical conductivities of liquid composites with various combinations.

4.7 Reliability test of the strain sensor through fruit model simulation

Samples with the liquid composites treated at different temperatures were tested on 3D-printed oval fruit models of varied sizes. Figure 4-13 shows the results of the measurement of resistance changes with diameters of 6.5, 7.5, and 8.5 cm. The 3D-printed oval fruit models and one with a digital LCR meter are shown in Figure 4-

13a-i and Figure 4-13a-ii respectively. The reliability test for the fruit model simulation was focused on the confirmation of long-term stability for the measurement of slowly changing lengths of objects such as fruits. Many of solid or liquid-state strain sensors have been developed for the short-term measurement of instantly changing resistance values caused by immediate deformation, elongation and compression while few research has been done to elucidate the long-term performance of strain sensors with high accuracy. Especially, no liquid-state sensors have been made and tested for the measurement of fruit growth. Each point on the graphs is the mean values of one-hour measurement with an interval of every second. The samples with the liquid composite treated at 70℃ for 4 hours (Figure 4-13d) showed standard deviations of 4.9 to 5.7 kΩ. The other samples with the non-heated liquid composite (Figure 4-13b) and with the liquid composite treated at 70℃ for 2 hours (Figure 4-13c) had standard deviations of 16.3 to 18.9 kΩ and of 8.4 to 11.0 kΩ respectively. The variations in absolute resistance values between the same types of samples were found to be the smallest for the samples with the composite treated at 70℃ for 4 hours. It is supposed that once the composite is heated at more than a certain temperature, the chemical stability of the composite increases through the aggregation of silver nanoparticles. Nevertheless, we confirmed that every sample with the differently treated composites showed a linear increase in resistance and similar increasing rates with respect to the circumference of the fruit models.

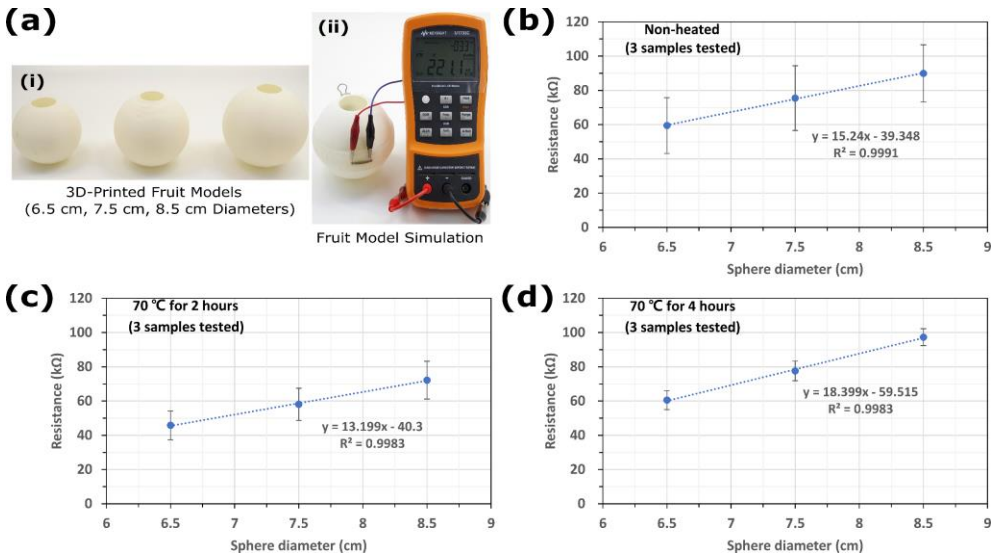

Figure 4-13. Reliability test using 3D-printed fruit models. 3 different samples were tested for each liquid composite. a) Experiment setup, i) 3D-printed oval fruit models. ii) Measurement system for the fruit model simulation. b) Samples with the non-heated liquid composite. c) Samples with the liquid composite treated at 70 ℃ for 2 hours. d) Samples with the liquid composite treated at 70℃ for 4 hours.

4.8 Continuous monitoring of real fruits with the strain sensor

After the fruit model simulation using the 3D-printed oval fruit models, the performance of the sensor as a dendrometer were tested on real fruits (Figure 4-14a-i). One thing to be noted is that the growth rate of the real fruits is slow and irregular with regard to the fixed velocities used during the previous stretching experiments with the syringe pump. Two distinct fruits with different rigidities were selected for the future implementation of the sensor to various fruits. Figure 4-14a-ii and Figure 4-14a-iii show a mandarin and a passion fruit respectively. Samples incorporated with the composite of PEG and silver nitrate treated at 70℃ for 2 hours were chosen for performance analysis as this type of samples showed

good characteristic stability on gauge factor and changes in resistance. The flexible bands that consist of the sensors were tuned differently depending on length to see the relationship between the degree of tightening and the increasing ratio of resistance. The initial circumferences of the mandarin and the passion fruit were 183 and 182 mm respectively. Figure 4-14b-i and Figure 4-14b-ii show resistance and circumference changes of the fruits for the first week. Based on the results of the previous experiments which proved that resistance changes are linearly proportional to elongation until the strain of 30%, circumference changes were calculated using resistance changes measured with the LCR meters. Each point on the graphs was plotted after calculating the mean values of one-hour recording of resistance with an interval of 30 seconds, which was primarily to eliminate insignificant and instant resistance fluctuations caused by miscellaneous factors inside the laboratory. The circumference of the mandarin increased from 183 to 192 mm while that of the passion fruit changed from 182 to 183 mm. The different growing growth rate might be due to the innate properties of the fruits. At the same time, the resistance of the flexible band attached on the mandarin increased from 20.8 to 35.9 kΩ with an increasing ratio of 1.7 kΩ/mm while that on the passion fruit was increasing from 19.3 to 23.2 kΩ with an increasing ratio of 3.9 kΩ/mm. For the second week of monitoring, the bands were loosened to alleviate the stress applied on the fruits and to watch a different aspect of resistance changes with different holes to fix the bands. The distance between each hole to fix the band was 6 mm. Figure 4-14c-i and Figure 4-14c-ii present resistance and circumference changes for the second week. The circumference of the mandarin changed from 192 to 196.5 mm while the resistance increased from 34.1 to 47.1 kΩ with an increasing ratio of 2.9 kΩ/mm. On the other hand, the circumference of the passion

fruit did not show distinguishable changes and the resistance oscillated between 23.0 and 22.1 kΩ. The different results observed from the two sensors on the fruits proved that the sensitivity and long-term stability of our stretchable strain sensor enable to detect resistance changes when fruits grow and to maintain stable resistance values when there is no significant volume expansion in fruits.

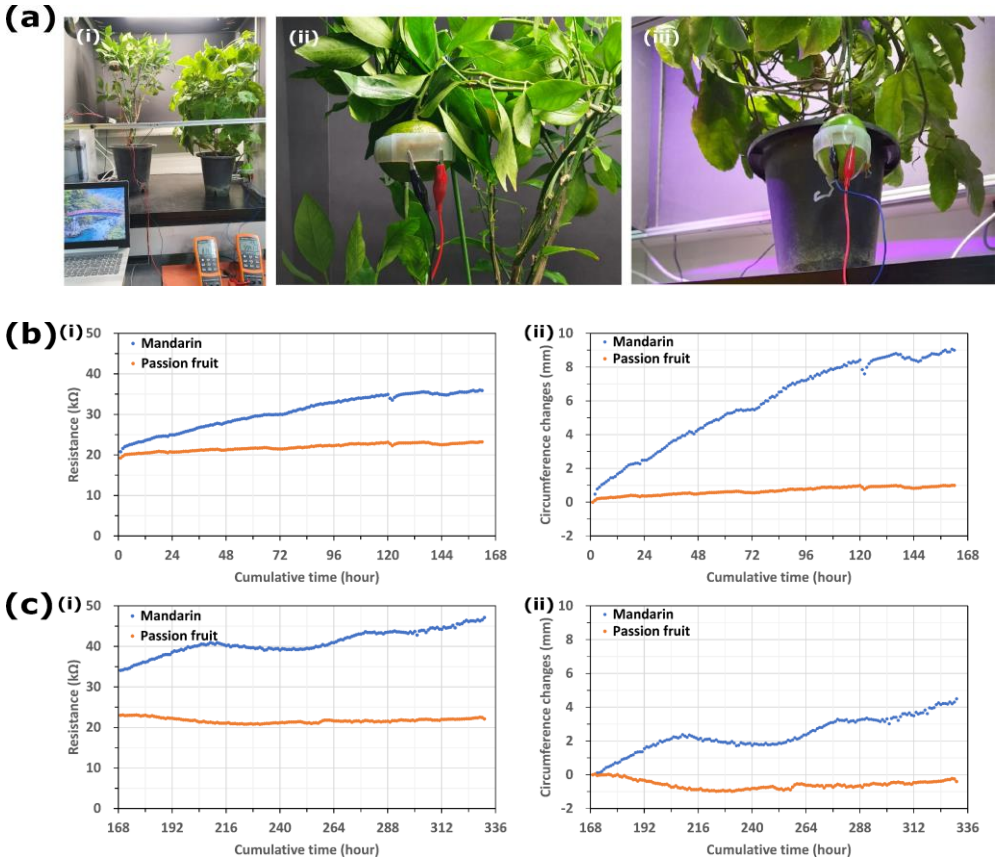

Figure 4-14. Real fruit growth monitoring using the stretchable strain sensor for fruit growth measurement. a) Experiment setup, i) Measurement system for fruit growth monitoring, ii) Mandarin sample, iii) Passion fruit sample. b) First week monitoring, (i) Time & resistance changes, (ii) Time & circumference changes. c) Second week monitoring, (i) Time & resistance changes, (ii) Time & circumference changes.

Chapter 5. Fabrication of a bio-inspired tactile sensor and its methods

I elaborated ideas towards a bio-inspired tactile sensor and its measurement system as shown in Figure 5-1. Usually, the principal unit of tactile sensors in insects roaming in the grass (Figure 5-1a-i) is the sensillum, which mainly consists of a cuticular apparatus represented by the hair called seta (Figure 5-1a-ii) [30]. I also present an antenna-shaped tactile sensor based on conductive liquid and elastomers as well as its measurement system (Figure 5-1a-iii, Figure 5-1-b).

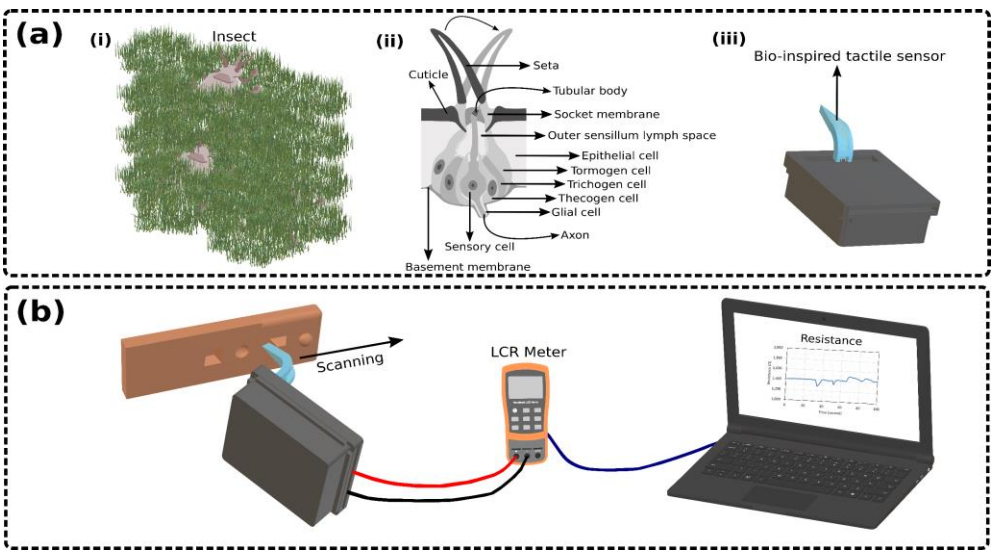

Figure 5-1. Schematic illustration of a bio-inspired tactile sensor. (a) Conceptual images of a bio-inspired tactile sensor, (i) Insects in the grass, (ii) Antenna of the insect, (iii) Device equipped with a bio-inspired tactile sensor. (b) Measurement system using a bio-inspired tactile sensor.

5.1 Fabrication a bio-inspired tactile sensor

The design of a mold with dimensions of 7 mm × 20 mm × 3 mm was conducted with AutoCAD 2020 before being printed out with a 3D printer (DP200, Sindoh). For the sensor structure, PDMS (Sylgard 184, Dow Corning) and its curing agent

were mixed with a ratio of 10:1. The part A and the part B of Ecoflex (00-30, Smooth-on) were blended with a ratio of 1:1. 20% of PDMS and 80% of Ecoflex were used to make a mixture of the two elastomers. For wall scanning test, other combinations (PDMS 60%/Ecoflex 40% and PDMS 40%/Ecoflex 60%) were also prepared. This mixture was kept in a centrifuge (Combi-514R, Hanil science industrial) for 4 minutes at 25 ℃, 200 μL of which was poured into the aforementioned 3D-printed mold before being shifted into an incubator (Thermo Scientific). After 4-hour heating at 45 ℃, the cured mixture of the elastomers was removed from the mold. The size of the sensor structure was 3 mm × 16 mm × 1.5 mm, and that of the channel to be filled with the liquid composite was 1.6 mm × 6.5 mm × 0.5 mm. 15 mm of Nichrome wires of 250 μm diameter were inserted from the bottom to the middle of the senor. 10 μL of the liquid composite was added after the plasma treatment of the channel for 25 seconds with a plasma processing equipment (CUTE, Femtoscience). Air bubbles in the liquid composite were eliminated in a vacuum desiccator (Lab Companion) for one hour. The uncured mixture of the elastomers was again used to cover the surface of the channel. After being stored for 2 hours at room temperature, the cover was hardened at 45℃ for 4 hours in the incubator to complete the fabrication of the bio-inspired tactile sensor.

5.2 Compatibility test using PEG, silver nitrate and sodium chloride

The structure for the compatibility test was deigned to be 36 mm × 16 mm × 1.75 mm with a channel of 19 mm × 3 mm × 0.5 mm using AutoCAD 2020 before being printed out with the 3D printer. The structure was made with a mixture of the

above-mentioned elastomers (PDMS 40%/Ecoflex 60%). At the same time, silver nitrate and sodium chloride (Sigma-Aldrich) were separately prepared in the range of 0.5 g to 1.5 g. Each combination was mixed with 2 mL of PEG. After 20-minute stirring at room temperature, every liquid composite was heated in the convection oven (Sanyo) at 70 ℃ for 2 hours. 55 μL of the liquid composites having been cooled down was poured into the channel of each sample whose cover was shortly hardened with the same mixture of the elastomers. For the measurement of each sample, resistance changes were recorded with a digital LCR meter (U1733C, Keysight) with an interval of every second at 1 KHz.

5.3 Fourier transform infrared (FTIR) spectrum analysis

The composites of PEG and silver nitrate treated at 70 ℃ for 2 hours and 4 hours were prepared as well as the non-heated liquid composite. 1 mL of each sample was used to realize the FTIR spectrum analysis with a FTIR spectrometer (TENSOR27, Bruker).

5.4 Measurement of silver nanoparticles in the liquid composites

2 mL of the composites of PEG and silver nitrate which were treated at different conditions (non-heated, 70℃ for 2 hours, and 70℃ for 4 hours) were made. After being kept in a cuvette, samples were analyzed in a particle size analyzer (Zetasizer Nano ZS, Malvern Instruments).

5.5 Simulations for the bio-inspired tactile sensor

The 3D-designed structure for the sensor whose size was 3 mm × 16 mm × 1.5 mm was designed with AutoCAD 2020 and used for simulations based on COMSOL Multiphysics. Young's modulus of the simulated structure was tested between 25 and 150 KPa while applied force was between 0 to 0.7 N.

5.6 Wall scanning tests with bio-inspired tactile sensors

Three walls were designed with AutoCAD 2020 with dimensions of 67.5 mm × 5 mm × 20 mm. The pyramidal structure whose height was 3 mm had the bottom of 6 mm × 6 mm as well as the top of 3 mm × 3 mm. The diameter of the hemisphere was 5 mm. A variety of combinations of the pyramidal structure and hemisphere of the same size were attached onto each wall before being printed out with the 3D printer while reverse structures of the same size were also added at the same time.

Chapter 6. Analysis of the bio-inspired tactile sensor

6.1 Compatibility test between PEG and silver nitrate

The fabrication process of the bio-inspired tactile sensor is briefly described in Figure 6-1. A mixture of PDMS and Ecoflex was used to make a sensor structure in combination with a 3D-printed mold (Figure 6-1a). Once the elastomer mixture was cured, the composite of PEG and silver nitrate was poured into the middle of the sensor structure in the presence of nichrome wires before being covered with the uncured elastomer mixture (Figure 6-1b). After heating the sensor structure, the uncured elastomer mixture was solidified while the liquid composite remained in a liquid state.

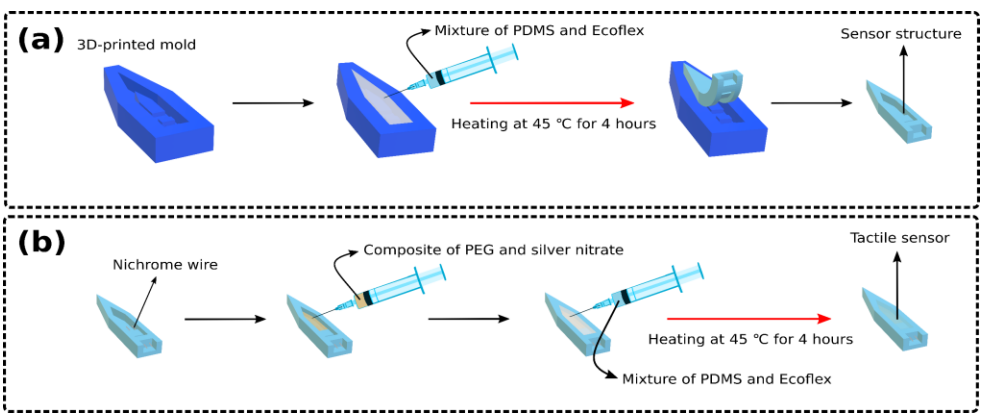

Figure 6-1. Fabrication process of the bio-inspired tactile sensor. (a) Preparation of a sensor structure using a mixture of PDMS and Ecoflex. (b) Completion of the bio-inspired tactile sensor with the encapsulation of a liquid composite of PEG and silver nitrate.

PEG often plays an important role as a stabilizer in various kinds of particles to prevent their aggregation and to maintain their chemical stability [56,57]. Given

that PEG is non-conductive material, the addition of electrolytes would be necessary to enhance the conductivity of the liquid. Metallic salts such as sodium chloride can be good electrolytes because they are easily dissociated in solution to create ions. However, if metallic salts are not compatible with PEG, they would not be well dissolved into PEG, which makes it complicated to supply ions in solution in a steady way. Moreover, undissolved particles could block the channel of the sensor where electric current is generated. For the analysis of the compatibility between PEG and metallic salts, I compared silver nitrate to sodium chloride which is one of the most common metallic salts (Figure 6-2). Each metallic salt was poured into the channel of a sample structure after being mixed with PEG. The quantity of the metallic salts was controlled from 0.5 g to 1.5 g while that of PEG was fixed at 2 mL. The resistance of each sample was measured with an interval of every second for one hour using a digital LCR meter. The result shows that as the amount of the metallic salts increased, the resistance of the liquid composites increased (Figure 6-2a). It is thought that without being ionized, the excessive amount of the metallic salts does not contribute to improving electric conductivity but to increasing the electrical resistance of the solutions. The difference between silver nitrate and sodium chloride is that resistance changes in the composite of PEG and silver nitrate were less abrupt than those in the composite of PEG and sodium chloride. At the same time, silver nitrate was found to be more soluble than sodium chloride in PEG (Figure 6-2b). The insolubility of sodium chloride might lead to the instability of the chemical properties of the liquid composite.

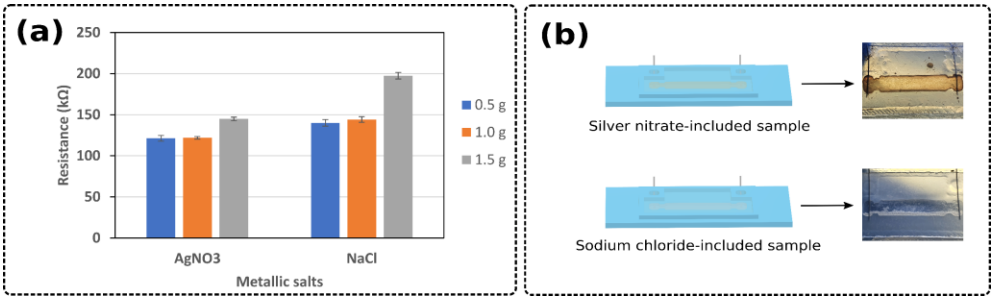

Figure 6-2. Compatibility test between PEG and different metallic salts. (a) Resistance measurement of the liquid composites made with silver nitrate and sodium chloride. (b) Preparation of the liquid composite samples and the images of their channels.

6.2 Chemical properties of PEG/silver nitrate composites

It was reported that when PEG and silver nitrate are mixed, the functional group of PEG is transformed into the aldehyde group [31]. Fourier transform infrared spectroscopy (FTIR) is often used to identify the presence of specific functional groups through molecular vibrations with thermal energy. For example, the interaction between silver nanoparticles and PEG was confirmed using this technique [34]. I investigated the FTIR spectrum of the composite of PEG and silver nitrate to verify chemical bonds present in the liquid composite (Figure 6-3). According to the result of the FTIR spectrum of the liquid composite and the infrared (IR) spectrum table, mainly O-H stretching, C-H stretching, C-H bending, and C-O stretching vibrations were found (Figure 6-3a). Especially, C-H stretching and bending vibrations might be related to the aldehyde group shown in Figure 6-3b. The absorption of frequencies caused by these vibrations can be good evidence to explain that the liquid composite would create the aldehyde group through the chemical reaction between PEG and silver nitrate.

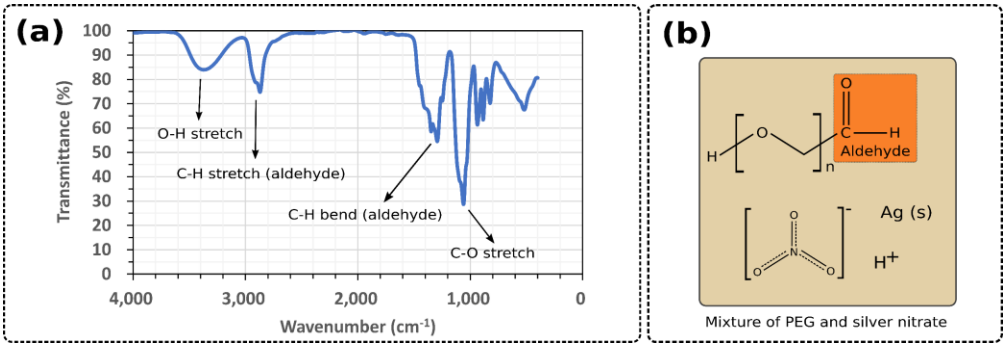

Figure 6-3. FTIR spectrum and the elements of the liquid composite. (a) FTIR spectrum of the composite of PEG and silver nitrate. (b) Elements of the liquid composite after mixing.

In addition to the confirmation of the chemical bonds using FTIR, I also conducted size measurement to see the distribution of silver particles in the mixture of PEG and silver nitrate (Figure 6-4). In this mixture, silver nitrate is reduced into silver particles whose size mainly depends on heating temperature [31]. The result obtained from a particle size analyzer in Figure 6-4d shows that most of silver particles in the non-heated liquid composite sample (Figure 6-4a) were located in the range of 0 to 1 μm while those in the liquid composite sample heated at 70 ℃ for 2 and 4 hours were in the range of 1 to 7 μm (Figure 6-4b, Figure 6-4c). The size measurement of silver particles enabled me to elucidate the chemical transition of the mixture of PEG and silver nitrate before and after being transformed into the liquid composite.

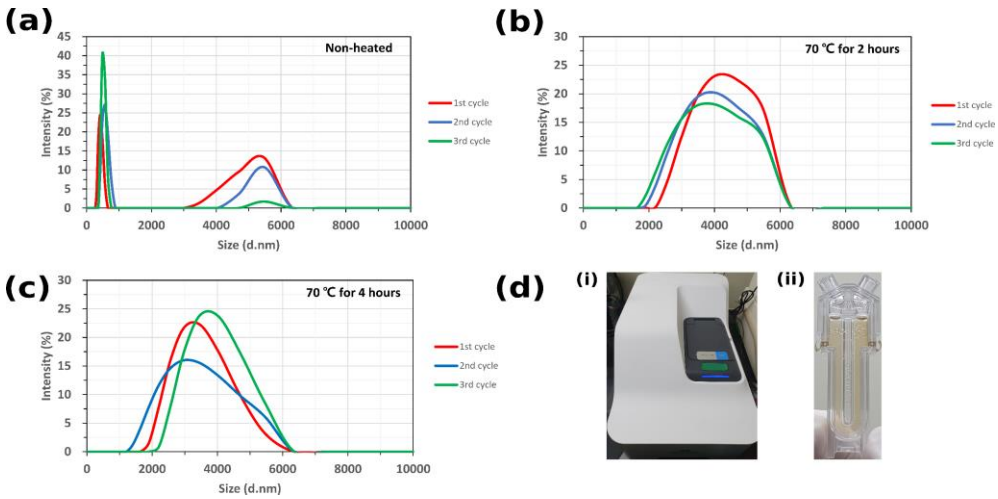

Figure 6-4. Size measurement of silver particles. Silver particles obtained (a) Without heating. (b) After being heated at 70 ℃ for 2 hours. (c) After being heated at 70 ℃ for 4 hours. (d) Measurement setup, (i) Particle size analyzer, (ii) Liquid composite sample in a cuvette.

6.3 Simulations of mechanical and electrical properties

Based on the 3D-designed structure of the bio-inspired tactile sensor, mechanical and electrical behaviors were simulated (Figure 6-5). For the analysis of mechanical properties, Young's modulus in the range of 25 to 150 KPa was tested while the influence of applied force on the sensor was examined in the range of 0 to 0.7 N (Figure 6-5a-i). A variety of Young's modulus represents the mixture of PDMS and Ecoflex with different mixing ratios. Electrical properties were also analyzed with the applied force of 0 to 0.5 N (Figure 6-5a-ii) to predict electric current between two nichrome wires. When the applied force was fixed at 0.15 N, the displacement of the tip of the bio-inspired tactile sensor was 4.8 mm at the Young's modulus 25 KPa and 0.9 mm at the Young's modulus of 150 KPa (Figure 6-5c). At the same time, when Young's modulus was set at 100 KPa, the tip of the

sensor followed linear displacements up to 5.5 mm with the increasing applied force up to 0.7 N (Figure 6-5d). Figure 6b presents cross section images of the sensor. As shown in Figure 6-5a-ii, most of electric current is generated mainly around the nearest path between two wire tips although ions are dispersed in the entire liquid composite. The volume of the liquid composite surrounding the nearest path between the wire tips is considered as one of the essential factors which would decide the resistance of the bio-inspired tactile sensor. Compared to the sensor in the initial state (Figure 6-5b-i), the sensor bent downwards would make larger space between the wire tips and the bottom of the liquid area, which could decrease electrical resistance (Figure 6-5b-ii). But the reduced space between the wire tips and the top of the liquid area would not increase electrical resistance up to a certain decree because this volume reduction might not be sufficient to affect the nearest path between the wire tips. If the sensor is bent more in the same direction enough to disturb the electric current generated along the nearest path, the total resistance could begin to increase. On the other hand, the sensor bent upwards would create narrower space between the wire tips and the bottom of the liquid area (Figure 6-5b-iii). In this case, the narrower gap between the tips and the bottom of the liquid area could increase electrical resistance due to the contraction of the nearest path for electric current in the liquid composite. However, the larger gap between the wire tips and the top of the liquid area might not have a significant effect on the total resistance because the excessive volume of the liquid composite surrounding the wire tips would have a less possibility of being occupied by electric current.

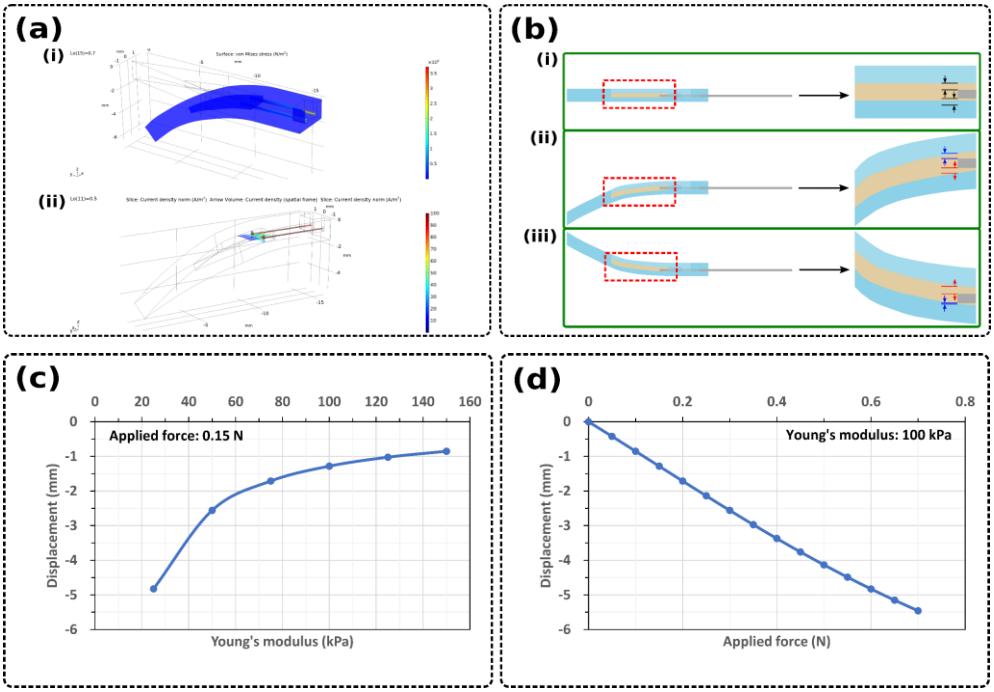

Figure 6-5. Simulations for mechanical and electrical properties of the bio-inspired tactile sensor. (a) Simulation results. (b) Cross section images of the sensor when being, (i) Flat, (ii) Bent downwards, (iii) Bent upwards. (c) Relationship between Young's modulus and displacement. d) Relationship between applied force and displacement.

6.4 Wall scanning test with the bio-inspired tactile sensor

The performance of the bio-inspired tactile sensor was tested using a 3D-printed wall with extruded and hollow hemispheres and pyramidal structures whose heights and depths were 2.5 mm and 3 mm respectively (Figure 6-6). The scanning speed was fixed at 400 μm/s using a syringe pump (Figure 6-6a-i). The distance between the bottom of the sensor and the flat area of the wall was maintained at 1.5 cm (Figure 6-6a-ii). If the distance between the sensor and an unknown object is given, the users can recognize not only the approximate distance between the sensor and the unknown object, but also realize its geographical reconstruction by

scanning techniques [58,59]. Figure 6-6a-iii presents the wall scanning sequence of the sensor. As shown in Figure 6-6b, the bio-inspired tactile sensor scanned the wall with varied bending angles, which were converted into resistance changes of the sensor. The size of the sensor was 3 mm × 16 mm × 1.5 mm (Figure 6-6c-i). The cross section of the sensor shows that the composite liquid remained intact without being affected by the solidification of the mixture of PDMS and Ecoflex (Figure 6-6c-ii). To understand the difference in tensile behavior between bio-inspired tactile sensors whose outer structure was made with different mixing ratios of PDMS and Ecoflex, three types of samples (PDMS 60%/Ecoflex 40%, PDMS 40%/Ecoflex 60%, PDMS 20%/Ecoflex 80%) were utilized for three times to calculate mean values (Figure 6-6d-i, Figure 6-6e-i, Figure 6-6f-i). The various mixing ratios of PDMS and Ecoflex was reported to change Young's modulus.[15] For all of the combinations, the sensors had higher sensitivities when they touched the extruded spots with a resolution of 500 μm. When the sensors scanned the hollow areas, their bending angles were almost negligible, which might lead to less sensitivities. The relationship between the bending angle and the resistance was scrutinized (Figure 6-6d-ii, Figure 6-6e-ii, Figure 6-6f-ii). The bending angle was calculated based on the location of the tip and the bottom of the sensor. The sensors with every combination show that changes in bending angle were generally proportional to those in resistance with the coefficients of determination of 0.9224 to 0.9889 up to 40 degrees. The sensitivity of the sensors was positioned in the range of 18 to 24 Ω/degree, which means that if the bending angle of the sensor is measured, the distance between the bottom of the sensor and unknown obstacles can be calculated. For geographical reconstruction, the relationship between the wall extrusion and the resistance was also analyzed, which also followed linear

behavior with the coefficients of determination of 0.9585 to 0.9947. Nevertheless, the diverse mixing ratios of PDMS and Ecoflex did not clarity specific tendency in mechanical properties of the sensors. It is assumed that the size of the sensors might not be big enough to indicate significant difference.

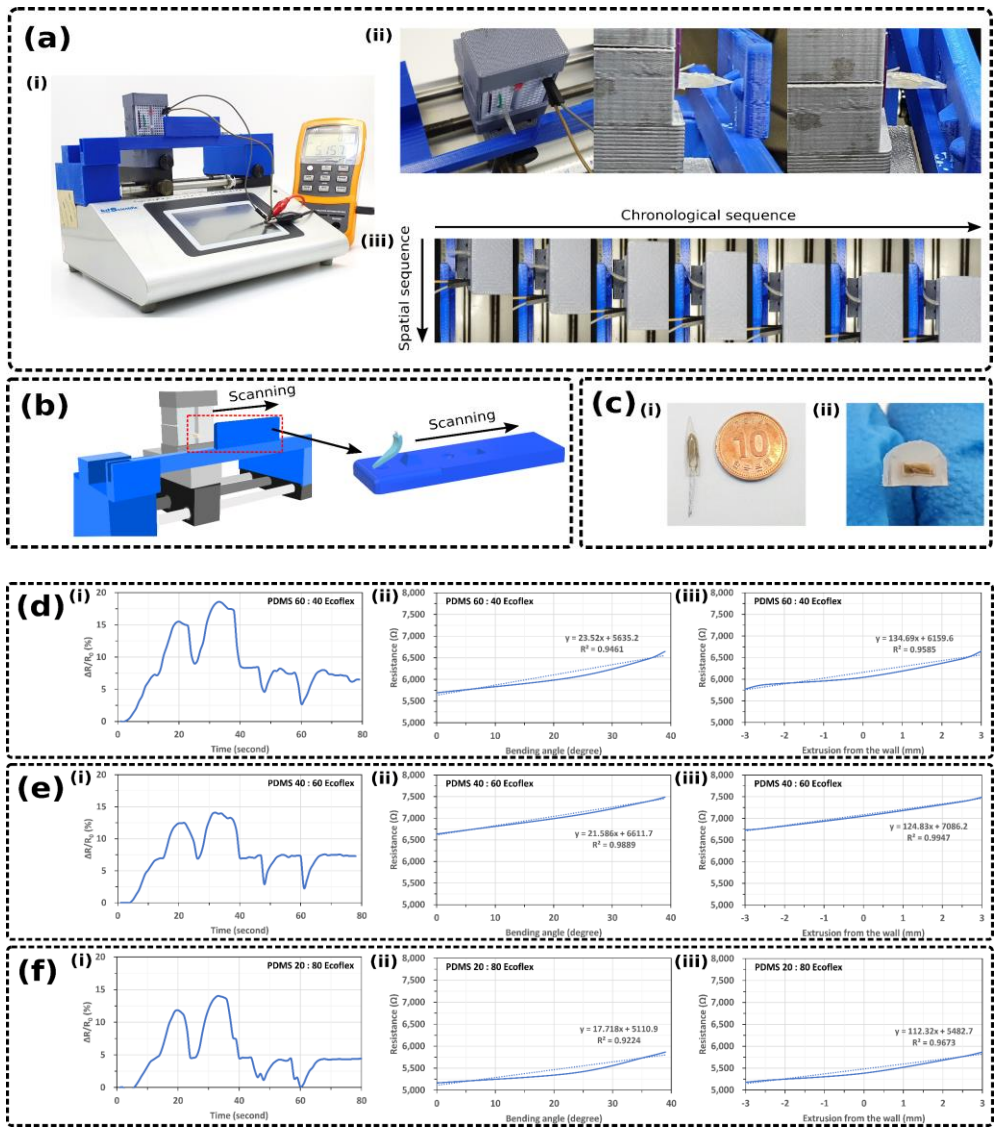

Figure 6-6. Characterization of the bio-inspired tactile sensor using a 3D-printed wall with various geometrical features. (a) Wall scanning test, (i) Experiment setup, (ii) Bio-inspired tactile sensor scanning the wall, (iii) Wall scanning sequence. (b) Illustration of the experiment setup. (c) Fabricated bio-inspired tactile sensor, (i) Sensor sample, (ii) Cross section image of the sensor. (d) Result of the wall scanning test (PDMS

60%/Ecoflex 40%). Relationships between (i) Time and resistance, (ii) Bending angle and resistance, (iii) Extrusion from the wall and resistance. (e) Result of the wall scanning test (PDMS 40%/Ecoflex 60%). Relationships between (i) Time and resistance, (ii) Bending angle and resistance, (iii) Extrusion from the wall and resistance. (f) Result of the wall scanning test (PDMS 20%/Ecoflex 80%). Relationships between (i) Time and Resistance, (ii) Bending angle and resistance, (iii) Extrusion from the wall and resistance.

6.5 Wall scanning test with multiple walls and multiple sensors

For the application of the bio-inspired tactile sensor in the field as part of a biomimetic robot, the reliability of multiple sensors facing unforeseeable obstacles needs to be guaranteed. Another wall scanning test was conducted for this purpose (Figure 6-7). I designed two walls in different shapes and two sensors were located between these two walls in opposite directions. The distance between the bottom of the sensor and the flat area of the wall was maintained at 1.5 cm for the both of the walls with the scanning speed of 400 μm/s (Figure 6-7a-i). Figure 6-7a-ii is the wall scanning sequence of the sensors. The walls were composed of extruded and hollow hemispheres and pyramidal structures whose heights and depths were 2.5 mm and 3 mm respectively (Figure 6-7a-iii, Figure 6-7a-iv). The geometrical features of the two walls were converted into the mean values of the resistance of the sensors after being scanned for three times (Figure 6-7b-i). The variations in absolute resistance values of each sensor might be due to the manual manufacturing process. Bending angles and wall extrusions were relatively proportional to the resistance with the coefficients of determination of 0.9011 to 0.9831.

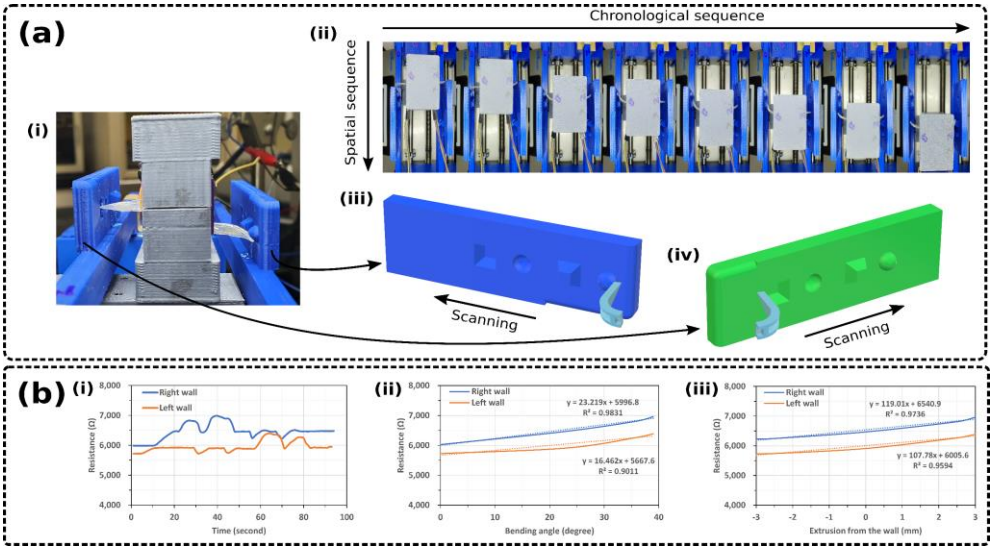

Figure 6-7. Characterization of multiple bio-inspired tactile sensor scanning multiple walls with distinct geometrical features. (a) Wall scanning test, (i) Bio-inspired sensors scanning two walls, (ii) Wall scanning sequence, (iii) Illustration of the left wall, (iv) Illustration of the right wall. (b) Result of multiple wall scanning test with multiple sensors. Relationships between (i) Time and resistance, (ii) Bending angle and resistance, (iii) Extrusion from the wall and resistance.

6.6 Wall scanning test with a single wall and multiple sensors

The installation of multiple sensors in many directions enables the users to gather as much information as possible. If the users locate a limited number of the sensors in the same direction, the accuracy of collected information would be improved because multiple sensors can scan a narrower area simultaneously. Figure 6-8 presents the whole process of the wall scanning test with a single wall and multiple sensors. The distance between the two sensors was about 5 mm while that between the bottom of the sensors and the wall was 1.5 cm (Figure 6-8a-i). As shown in the illustration (Figure 6-8a-iii), two sensors installed in the same direction moved for three times in front the wall with the scanning speed of 400 μm/s (Figure 6-8a-ii).

Although some variations in absolute resistance values were found after calculating mean values, each sensor could express the detailed geometrical characteristics of the wall (Figure 6-8b-i). However, the proportionality between the bending angle and the resistance as well as between the wall extrusion and the resistance was not as well maintained as in the previous experiments. These aberrant results might be caused by manual errors during the test. Nevertheless, throughout the three different wall scanning experiments, our bio-inspired tactile sensor showed the resistance highly proportional to the bending angle and the wall extrusion.

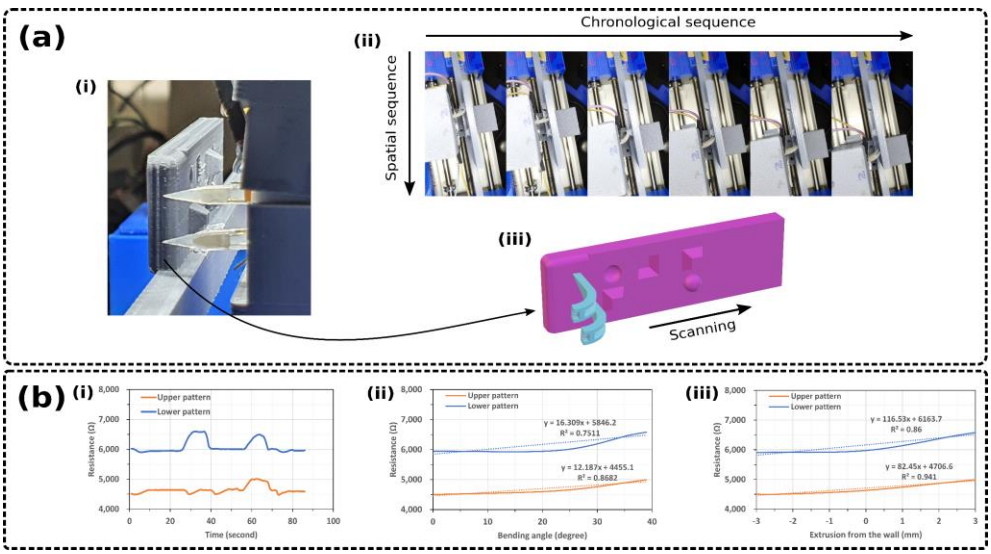

Figure 6-8. Characterization of multiple bio-inspired tactile sensors scanning a single wall. (a) Wall scanning test, (i) Experiment setup, (ii) Wall scanning sequence, (iii) Illustration of the wall. (b) Result of a single wall scanning test with multiple sensors. Relationships between (i) Time and resistance, (ii) Bending angle and resistance, (iii) Extrusion from the wall and resistance.

6.7 Geographical reconstruction

The relationship between the bending angle and the resistance informs the users of the presence of unknown obstacles often in the form of wall. I also collected information about the distance between the wall extrusion and the resistance to

realize geometrical reconstruction. Trend lines extracted from the proportional relationship between the bending angle and the resistance as well as that between the wall extrusion and the resistance can be used. Two of the previously shown results of the wall scanning tests were taken (Figure 6-6e-i, Figure 6-7b-i) for further analysis. Figure 6-9 is the result of a geometrical reconstruction based on two different methods of calculation. The first reconstructed pattern was directly calculated from the trend line of Figure 6-6e-iii while the second reconstructed pattern was from the both of the trend lines of Figure 6-7e-ii and Figure 6-7e-iii (Figure 6-9a-i). The establishment of the relationship between the bending angle and the wall extrusion was also carried out before geometrical reconstruction. The measurement of the bending angle allows the users to recognize whether the sensor touches the wall or not. However, the bending angle cannot easily detect hollow areas in case the distance between the bottom of the sensor and the flat area of the wall is fixed. On the other hand, the measurement of the wall extrusion enables the users to collect detailed information about extruded and hollow geometrical features. But this method would not be available if the sensor touches no obstacle. For this reason, I decided to combine these two methods of calculation. Figure 10a-ii is the wall was designed for geometrical reconstruction. Compared to the first reconstructed pattern, the second reconstructed pattern was realized with higher accuracy especially in the level of the flat area of the wall. The result from the multiple wall scanning was also converted into reconstructed geometry using the two calculating methods (Figure 10b-i). The heights and depths of each spot were maintained between 2.5 mm for the hemispheres and 3.0 mm for the pyramidal structures (Figure b-ii). The reconstructed features of the two walls surrounding the sensor was presented with high accuracy. I found that the higher the coefficient of

determination from wall scanning tests is, the more accurate the geometrical reconstruction process is. Therefore, it was proved that this calculating tool using the trend line can be employed to reconstruct the geometrical features of unexpected obstacles.

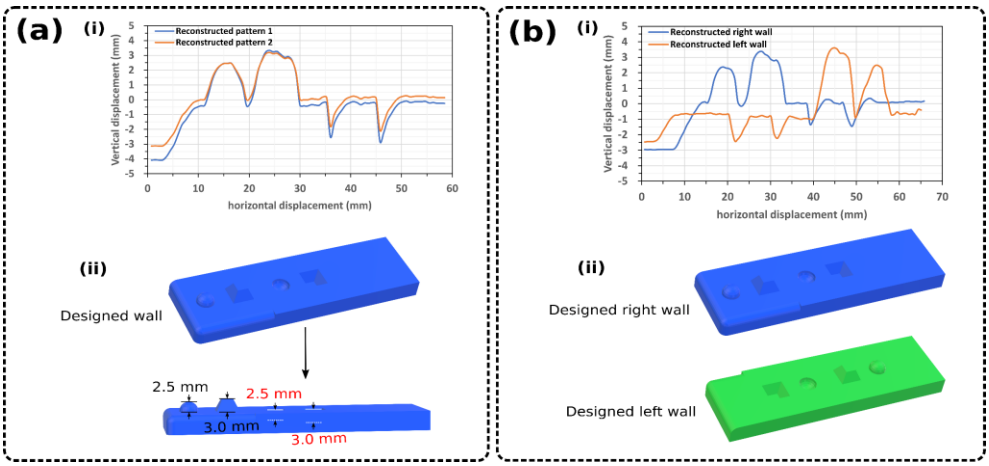

Figure 6-9. Reconstruction of the geographical features of the scanned wall. (a) Geographical reconstruction with a single wall, (i) Result of the reconstructed structure. (ii) Illustration of the designed wall. (b) Geographical reconstruction with multiple walls, (i) Result of the reconstructed structures. (ii) Illustration of the designed walls.

Chapter 7. Discussion

7.1 Temperature compensation of the stretchable strain sensor

For the accurate calculation of the circumference of fruits by the change in resistance, the resistance has to be the only parameter which decides the circumference. Other factors which can interfere in the conversion of resistance into the circumference are mainly temperature and humidity. That is why I conducted the monitoring of real fruits with controlled temperature and humidity. In order to eliminate the interference of these factors, several options would be available. Firstly, the sensor could be used in a controlled environment such as a greenhouse. For this, we would be able to make sure that resistances changes are only due to fruit growth. Secondly, when it comes to the temperature, the temperature compensation of the sensor could be realized with a supplementary resistor whose temperature coefficient of resistance (TCR) is opposite to that of the sensor. Figure 7-1 is the result of a temperature compensation test. Lastly, recording the resistance at periodic intervals of temperature and humidity would be available to calculate the circumference of fruits. Compared to other strain sensors whose goal is often to measure the instant movement of an object, my sensor is made for long-term measurement. Moreover, it usually takes several weeks for fruits to growth. In this case, the addition of a thermo-hygrometer would be a solution to collect a sufficient amount of resistance data with specific conditions.

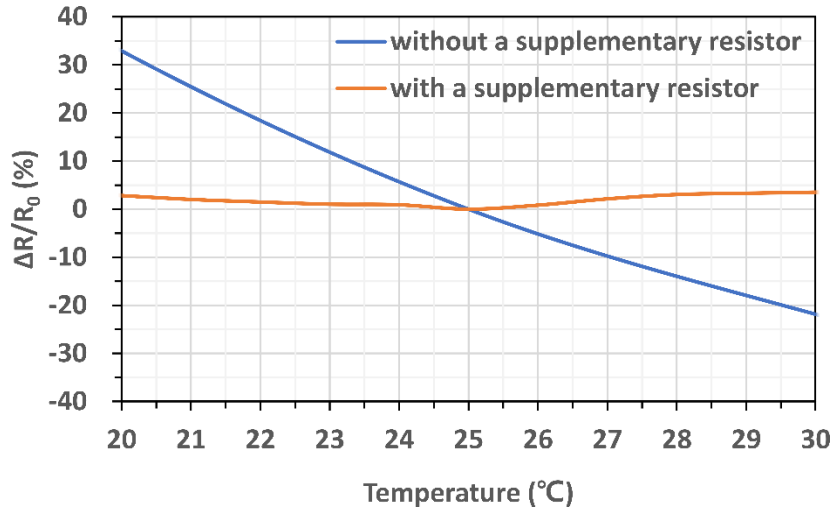

Figure 7-1. Temperature compensation of the sensor with a supplementary resistor made with graphene powder

7.2 Portable power supplier for the stretchable strain sensor and the bio-inspired tactile sensor

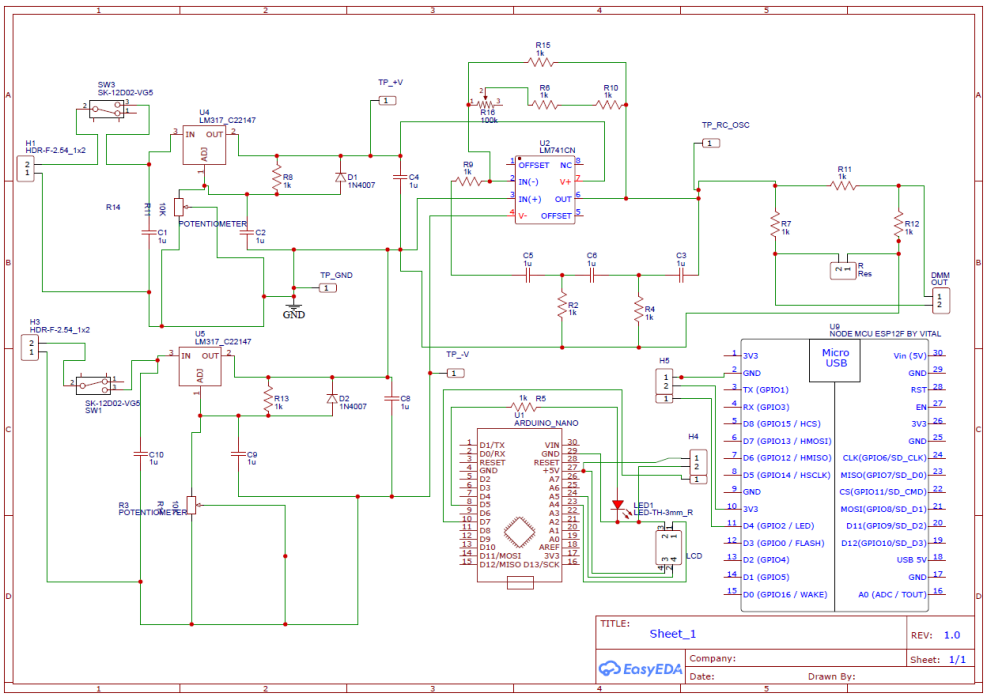

Figure 7-2. Circuit diagram of the portable power supplier

Technically, it is not easy to attach the sensor to every fruit even though it would be an effective way to collect as much data as possible. As an alternative way, it could be a solution to install strain sensors to certain fruits which can represent those in the same local conditions such as local temperature, local humidity, local light intensity, etc. The sampling of fruits would be able to reduce considerably the number of the sensors needed for growth monitoring. For the purpose of field application, I designed a portable electronic circuit generating 1 KHz and 1 V_{pp} signal from an RC phase shift oscillator, which could be combined with wireless communication to realize IoT-based long-term fruit growth monitoring. The circuit diagram is shown in Figure 7-2, and the portable power supplier was assembled (Figure 7-3). In this circuit, the resistance from the sensor is set to be the variable resistor of a Wheatstone's bridge having three identical resistors of 100 KΩ. Then, changes in voltage extracted from the balanced bridge could be transformed into those in fruit circumference. Based on the result obtained from the two-week fruit growth monitoring and my portable electronic circuit, I believe that the collection of the electrical resistance information for long-term would be possible to effectively monitor fruit growth.

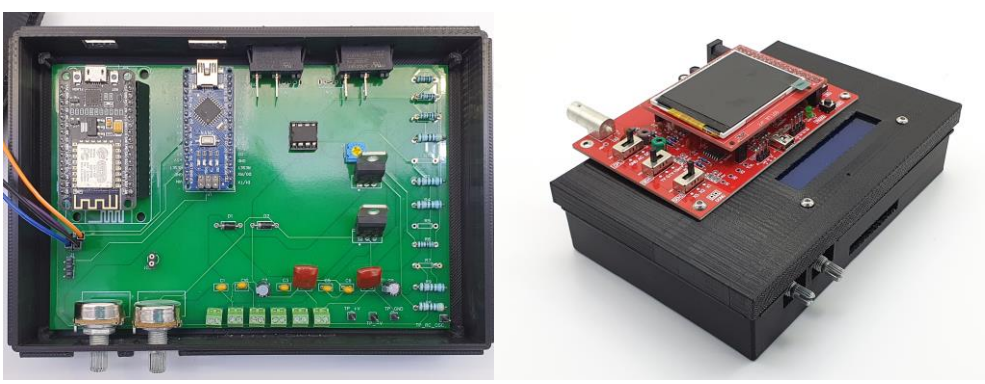

Figure 7-3. Circuit diagram of the portable power supplier (left) and the packaged portable power supplier

7.3 Future work

The development of the liquid polymer/metallic salt-based stretchable strain sensor and the antenna-shaped biomimetic tactile sensor would be able to lead to further research to improve their performance. For example, if we find alternative liquid

materials which have lower TCRs, these sensors would be less affected by temperature variations. The elaboration of an effective method to compensate temperature-dependent resistance values could be also an interesting research topic. The investigation of an IoT-based long-term monitoring system for fruit growth combined with these sensors and the portable power supplier would be able to bring fruitful results for field application. The integration of the tactile sensor into a biomimetic robot would be able to prove its possibility to function as an efficient artificial tactile sensing system in the presence of other sensory systems.

Chapter 8. Conclusion

In summary, my liquid polymer/metallic salt-based stretchable strain sensor was realized with a composite of PEG and silver nitrate and using an encapsulation technique based on the chemical properties of each substance. Compared to other liquid-state strain sensors, the low-cost composite of our sensor takes advantage of high viscosity and chemical stability from a liquid polymer and of enhanced conductivity from metallic salt-driven electrolytes at the same time. The 3D designing and printing methods facilitated the fabrication of the entire sensor including the easily tunable elastic band which could be adapted to the size and shape of various fruit species. The analysis of the composite treated at different temperatures enabled to find that the formation of silver nanoparticles is not directly relevant to the electrical resistance of the composite. In addition, heating the composite is supposed to increase chemical stability to a certain degree in comparison with the non-heated composite although the composite treated at excessively high temperature hindered the appropriate hardening of the aqueous elastomers on the top of the sensor. I observed linear proportional increments of resistance with respect to the stretching and releasing of the sensor at least until the strain of 30%. The two distinct silicon-based elastomers with diverse ratios allowed me to identify the optimal mixing ratio of the elastomers which can achieve the equilibrium between large strain, low stress and less stickiness. Finally, the fruit model simulation and the continuous monitoring with real fruits contributed to the confirmation of the possibility of my sensor as a long-time measurement method for more than one week and as a liquid-based dendrometer which is adjustable to fruits of varied sizes and shapes. Accordingly, my stretchable strain sensor with

high sensitivity, good repeatability and excellent stability presents a novel perspective on liquid-state strain sensors represented by the use of new materials, long-term measurement, and a new approach to other fields.

At the same time, my bio-inspired tactile sensor was inspired by the sensory structure of an insect which controls the tactile sensing system. The encapsulation of the composite of PEG and silver nitrate in the mixture of elastomers in combination with nichrome wires gave shape to a biomimetic tactile sensor represented by the seta, outer sensillum lymph space, tubular body and sensory cell. Compared to other solid-state tactile sensors, the resistance of our sensor when being bent is believed to be decided by the positioning of wires in the liquid composite as well as the distribution of the liquid composite covering the nearest path for the generation of electric current. The wall scanning experiments at a fixed speed and a fixed distance with the sensor revealed the resolution of 500 μm in depth of the sensor. The combination of 3D-printed obstacles in various shapes and the installation of multiple sensors in diverse directions established a proportional relationship between the bending angle and the resistance with high coefficients of determination at least up to 40-degree bending. The geometrical reconstruction using the combination of the relationships between the bending angle and the resistance, between the bending angle and the wall extrusion, and the wall extrusion and the resistance showed the possibility of further research for 3D image reconstruction. I believe that the newly developed bio-inspired tactile sensor would be able to be integrated to a biomimetic robot as an alternative apparatus to detect visual information as well as a mechanoreceptor to sense vibration, avoid collisions and recognize external stimuli.

Bibliography

[1] Chong, H. Lou, J.; Bogie, K. M.; Zorman, C. A.; Majerus, S. J. A. Vascular Pressure-Flow Measurement Using CB-PDMS Flexible Strain Sensor. *IEEE Trans. Biomed. Circuits Syst.* **2019**, *13*, 1451-1461.

[2] Li, Z. Y.; Zhai, W.; Yu, Y. F.; Li, G. J.; Zhan, P. F.; Xu, J. W.; Zheng, G. Q.; Dai, K.; Liu, C. T.; Shen, C. Y. An Ultrasensitive, Durable and Stretchable Strain Sensor with Crack-Wrinkle Structure for Human Motion Monitoring. *Chin. J. Polym. Sci.* **2020**, *39*, 316-326.

[3] Amjadi, M.; Pichitpajongkit, A.; Lee, S.; Ryu, S.; Park, I. Highly Stretchable and Sensitive Strain Sensor Based on Silver Nanowire – Elastomer Nanocomposite. *ACS Nano* **2014**, *8*, 5154-5163.

[4] Li, J.; Zhao, S.; Zeng, X.; Huang, W.; Gong, Z.; Zhang, G.; Sun, R.; Wong, C. P. Highly Stretchable and Sensitive Strain Sensor Based on Facilely Prepared Three-Dimensional Graphene Foam Composite. *ACS Appl. Mater. Interfaces* **2016**, *8*, 18954-18961.

[5] Qi, Z.; Bian, H.; Yang, Y.; Nie, N.; Wang, Fuliang. Graphene/Glycerin Solution-Based Multifuncional Stretchable Strain Sensor with Ultra-High Stretchability, Stability and Sensitivity. *Nanomaterials*. **2019**, *9*, 617.

[6] Xu, M.; Qi, J.; Li, F.; Zhang, Y. Highly Stretchable Strain Sensors with Reduced Graphene Oxide Sensing Liquids for Wearable Electronics. *Nanoscale* **2018**, *10*, 5264-5271.

[7] Russo, S.; Ranzani, T.; Liu, H.; Nefti-Meziani, S.; Althoefer K.; Menciassi, A. Soft and Stretchable Sensor Using Biocompatible Electrodes and Liquid for Medical Applications. *Soft Rob.* **2015**, *2*, 146-154.

[8] Matsuzaki, R.; Tabayashi, K. Highly Stretchable, Global, and Distributed Local Strain Sensing Line Using GaInSn Electrodes for Wearable Electronics, *Adv. Funct. Mater.* **2015**, *25*, 3806-3813.

[9] Liu, C.; Han, S.; Xu, H.; Wu, J.; Liu, C. Multifunctional Highly Sensitive Multiscale Stretchable Strain Sensor Based on a Graphene/Glycerol-KCl Synergistic Conductive Network. *ACS Appl. Mater. Interfaces* **2018**, *10*, 31716-31724.

[10] Yoon, S. G.; Koo, H. J.; Chang, S. T. Highly Stretchable and Transparent Microfluidic Strain Sensor for Monitoring Human Body Motions. *ACS Appl. Mater. Interfaces* **2015**, *7*, 27562-27570.

[11] Key, F. S.; Maass, G. Determining the Properties of Colloidal Silver. *Silver Colloids* **2001**.

[12] Link, S. O.; Thiede, M. E.; van Bavel, M. G. An Improved Strain-Gauge Device for Continuous Field Measurement of Stem and Fruit Diameter. *J. Exp. Bot.* **1998**, *49*, 1583-1587.

[13] Yoda, K.; Suzuki, M.; Suzuki, H. Development and Evaluation of a New Type of Opto-Electronic Dendrometer. *IAWA Journal* **2000**, *21*, 425-434.

[14] Uchida, H.; Akita, S.; Kumekawa, N.; Watanabe K. A Hetero-Core Optical Fiber Dendrometer for Measurement of a Tree Growing Condition. *ICCAS* **2010**.

[15] Just, M. G.; Frank, S. D. Evaluation of an Easy-to-Install, Low-Cost Dendrometer Band for Citizen-Science Tree Research. *J. For.* **2019**, *117*, 317-322.

[16] Anemaet, E. R.; Middleton, B. A. Dendrometer Bands Made Easy: Using Modified Cable Ties to Measure Incremental Growth of Trees. *Appl. in Plant Sci.* **2013**, *1*, 1-5.

[17] Back, S.-H.; Kim, D.-E. Microphone-Based Whisker Tactile Sensors

Modeling Rodent Whiskers. *The Journal of Korea Robotics Society* **2009**, *4*, 34-42.

[18] Hires, S. A.; Pammer, L.; Svoboda, K.; Golomb, D. Tapered whiskers are required for active tactile sensation. *eLife* **2013**, *2*, e01350.

[19] Feliu-Batlle, V.; Feliu-Talegon, D.; Castillo-Berrio, C. F. Improved Object Detection Using a Robotic Sensing Antenna with Vibration Damping Control. *Sensors* **2017**, *17*, 852.

[20] Nguyen, T.-D.; Lee, J. S. Recent Development of Flexible Tactile Sensors and Their Applications. Sensors **2022**, *22*, 50.

[21] Sayegh, M.-A.; Daraghma, H.; Mekid, S.; Bashmal, S. Review of Recent Bio-Inspired Design and Manufacturing of Whisker Tactile Sensors. *Sensors* **2022**, *22*, 2705.

[22] Patanè, L.; Hellbach, S.; Krause, A.; Arena, P.; Dürr, V. An insect-inspired bionic sensor for tactile localization and material classification with state-dependent modulation. *Frontiers in Neurorobotics* **2012**, *6*.

[23] Prescott, T. J.; Diamond, M. E.; Wing, A. M. Active touch sensing. *Phil. Trans. R. Soc. B* **2011**, *366*, 2989-2995.

[24] Baba, Y.; Tsukada, A.; Comer, C. M. Collision avoidance by running insects: antennal guidance in cockroaches. *J. Exp. Biol.* **2010**, *213*, 2294-2302.

[25] Mongeau, J.-M.; Demir, A.; Lee, J.; Cowan, N. J.; Full, R. J. Locomotion- and mechanics-mediated tactile sensing: antenna reconfiguration simplifies control during high-speed navigation in cockroaches. *J. Exp. Biol.* **2013**, *216*, 4530-4541.

[26] Oka, H.; Terao, K.; Shimokawa, F.; Takao, H. An Antenna-Shaped MEMS Tactile Sensor with Angle Detection Capability. *IEEE 34th International Conference on Micro Electro Mechanical Systems (MEMS)* **2021**, 139-142.

[27] Alfadhel, A.; Kosel, J. Magnetic Nanocomposite Cilia Tactile Sensor. *Adv.*

Mater. **2015**, *27*, 7888-7892.

[28] Wu, Z.; Ai. J.; Ma Z.; Zhang, X.; Du, Z.; Liu, Z.; Chen, D.; Su, B. Flexible Out-of Plane Wind Sensors with a Self-Powered Feature Inspired by Fine Hairs of the Spider. *ACS Appl. Mater. Interfaces* **2019**, *11*, 44865-44873.

[29] Chakilam, S.; L, D. T.; Xi, Z. C.; Gaidys, R.; Lupeikiene, A. Morphological Study of Insect Mechanoreceptors to Develop Artificial Bio-Inspired Mechanosensors. *Engineering Proceedings* **2020**, *2*, 70.

[30] Keil, T. A. Functional morphology of insect mechanoreceptors. *Microsc. Res. Tech.* **1997**, *39*, 506-531.

[31] Lee, H. J.; Joyce, R.; Lee, J. Liquid Polymer/Metallic Salt-Based Stretchable Strain Sensor to Evaluate Fruit Growth. *ACS Appl. Mater. Interfaces* **2022**, *14*, 5983-5994.

[32] Luo, C.; Zhang, Y.; Zeng, X.; Zeng, Y.; Wang, Y. The role of poly(ethylene glycol) in the formation of silver nanoparticles. *J. Colloid Interface Sci.* **2005**, *288*, 444-448.

[33] Popa, M.; Pradell, T.; Crespo, D.; Calderón-Moreno, J. M. Stable silver colloidal dispersons using short chain polyethylene glycol. Colloid Surf., A **2007**, *303*, 184-190.

[34] Shameli, K.; Ahmad, M. B.; Jazayeri, S. D.; Sedaghat, S.; Shabanzadeh, P.; Jahangirian, H.; Mahdavi, M.; Abdollahi, Y. Synthesis and Characterization of Polyethylene Glycol Mediated Silver Nanoparticles by the Green Method. *Int. J. Mol. Sci.* **2012**, *13*, 6639-6650.

[35] Liang, W.; Wang, L.; Zhu, Z.; Qian, C.; Sun, H.; Yang, B.; Li, A. *In Situ* Preparation of Polyethylene Glygol/ Silver Nanoparticles Composite Phase Change

Materials with Enhanced Thermal Conductivity. *ChemistrySelect* **2017**, *2*, 3428-3436.

[36] Dorjnamjin, D.; Ariunaa, M.; Shim, Y. K. Synthesis of Silver Nanoparticles Using Hydroxyl Functionalized Ionic Liquids and Their Antimicrobial Activity. *Int. J. Mol. Sci.* **2008**, *9*, 807-820.

[37] Choi, D. Y.; Kim, M. H.; Oh, Y. S.; Jung, S. H.; Jung J. H.; Sung, H. J.; Lee, H. W.; Lee, H. M. Highly Stretchable, Hysteresis-Free Ionic Liquid-Based Strain Sensor for Precise Human Motion Monitoring, *ACS Appl. Mater. Interfaces* **2017**, *9*, 1770-1780.

[38] Hess, M.; Jones, R. G.; Kahovec J.; Kitayama, T.; Kratochvil, P.; Kubisa, P.; Mormann, W.; Stepto, R. F. T.; Tabak, D.; Vohlidal, J.; Wilks, E. S. Terminology of Polymers Containing Ionizable or Ionic Groups and of Polymers Containing Ions. *Pure Appl. Chem.* **2009**, *78*, 2067-2074.

[39] Michaels, A. S. Polyelectrolyte Complexes, *Industrial and Engineering Chemistry* **1965**.

[40] Wang, Y.; Gong, S.; Wang, S. J.; Simon G. P.; Cheng, W. Volume-Invariant Ionic Liquid Microbands As Highly Durable Wearable Biomedical Sensors. *Mater. Horiz.* **2016**, *3*, 208-213.

[41] Keulemans, G.; Pelgrims, P.; Bakula, M.; Ceyssens, F.; Puers, R. An Ionic Liquid Based Strain Sensor for Large Displacements. *Procedia Eng.* **2014**, *87*, 1123-1126.

[42] Chossat, J. B.; Park, Y. L.; Wood, R. J.; Duchaine, V. A Soft Strain Sensor Based on Ionic and Metal Liquids. *IEEE Sens. J.* **2015**, *13(9)*, 3405-3414.

[43] Zhu, Y.; Chao, C.; Cheng, C. H.; Leung, W. W. F. A Novel Ionic-Liquid Strain Sensor for Large-Strain Applications. *IEEE Electron Device Lett.* **2009**, *30*, 337-339.

[44] Park, E. J.; Cho, Y. K.; Kim, D. H.; Jeong, M. G.; Kim, Y. H.; Kim, Y. D. Hydrophobic Polydimethylsiloxane (PDMS) Coating of Mesoporous Silica and Its Use As a Preconcentrating Agent of Gas Analytes. *Langmuir* **2014**, *30*, 10256-10262.

[45] Lu, Z.; Song, J.; Pan, K.; Meng, J.; Xin, Z.; Liu, Y.; Zhao, Z.; Gong, R. H.; Li, J. EcoFlex Sponge with Ultrahigh Oil Absorption Capacity. *Appl. Mater. Interfaces* **2019**, *11*, 20037-20044.

[46] Lai, H.; Wu, P. Hydration Capabilities and Structures of Carbonyl and Ether Groups in Poly(3-(2-methoxyethyl)-N-vinyl-2-pyrrolidone) Film. *Polym. Chem.* **2013**, *4*, 3323-3332.

[47] Sagawa, N.; Shikata T. Are All Polar Molecules Hydrophilic? Hydration Numbers of Nitro Compounds and Nitriles in Aqueous Solution. *Phys. Chem. Chem. Phys.* **2014**, *16*, 13262-13270.

[48] Fawcett, A. S.; So, H. Y.; Brook, M. A. Silicone Foams Stabilized by Surfactants Generated *in situ* From Allyl-functionalized PEG. *Soft Matter* **2010**, *6*, 1229-1237.

[49] Lewis, L. N.; Stein J.; Gao, Y.; Colborn, R. E.; Hutchins, G. Platinum Catalysts Used in the Silicones Industry. *Platinum Met. Rev.* **1997**, *41*, 66-75.

[50] Sturgess, C.; Tuck, C. J.; Ashcroft, I. A.; Wildman, R. D. 3D Reactive Inkjet Printing of Polydimethylsiloxane. *J. Mater. Chem. C* **2017**, *5*, 9733-9743.

[51] Fleitas-Salazar, N.; Silva-Campa, E.; Pedroso-Santana, S.; Tanori, J.; Pedroza-Montero, M. R.; Riera, R. Effect of Temperature on the Synthesis of Silver

Nanoparticles with Polyethylene Glycol: New Insights into the Reduction Mechanism. *J. Nanopart. Res.* **2017**, *19*, 1-12.

[52] Lee, W. J.; Park, S. Y.; Nam, H. J.; Choa, S. H. Mechanical and Optical Characteristics of Transparent Stretchable Hybrid Substrate using PDMS and Ecoflex Material. *J. Microelectron. Packag. Soc.* **2018**, *25*, 129-135.

[53] De Leersnyder, I.; De Gelder, L.; Van Driessche, I. ; Vermeir, P. Revealing the Importance of Aging, Environment, Size and Stabilization Mechanisms on the Stability of Metal Nanoparticles : A Case Study for Silver Nanoparticles in a Minimally Defined and Complex Undefined Bacterial Growth Medium. *Nanomaterials.* **2019**, *9*, 1684-1703.

[54] Patel, K.; Deshpande, M. P.; Gujarati, V. P.; Chaki S. H. Effect of Heating Time Duration on Synthesis of Colloidal Silver Nanoparticles. *Adv. Mater. Res.* **2016**, *1141*, 14-18.

[55] Laroo, H. Colloidal Nano Silver-Its Production Method, Properties, Standards and Its Bio-Efficacy As an Inorganic Antibiotic. *J. Phys. Chem. Biophys.* **2013**, *3*, 1-9.

[56] Castellanos, I. J.; Crespo, R.; Griebenow, K. Poly(ethylene glycol) as stabilizer and emulsifying agent: a novel stabilization approach preventing aggregation and inactivation of proteins upon encapsulation in bioerodible polyester microspheres. *J. Controlled Release* **2003**, *88*, 135-145.

[57] Péan, J.-M.; Boury, F.; Venier-Julienne, M.-C.; Menei, P.; Proust, J.-E.; Benoit, J.-P. Why Does PEG 400 Co-Encapsulation Improve NGF Stability and Release from PLGA Biodegradable Microspheres? *Pharm. Res.* **1999**, *16*, 1294-1299.

[58] Harada, S.; Honda, W.; Arie, T.; Akita, S.; Takei, K. Fully Printed, Highly Sensitive Multifunctional Artificial Electronic Whisker Arrays Integrated with Strain and Temperature Sensors. *ACS Nano* **2014**, *8*, 3921-3927.

[59] Hua, Q.; Liu, H.; Zhao, J.; Peng, D.; Yang, X.; Gu, L.; Pan, C. Bioinspired Electronic Whisker Arrays by Pencil-Drawn Paper for Adaptive Tactile Sensing. *Adv. Electron. Mater.* **2016**, *2*, 1600093.

[60] Bu, H.; Yu, W.; Yuan, H.; Yue, P.; Wei, Y.; Wang, A. Endogenous Auxin Content Contributes to Larger Size of Apple Fruit. *Front. Plant Sci.* **2020**, *11*, 592540.

[61] Bertin, N. Analysis of the Tomato Fruit Growth Response to Temperature and Plant Fruit Load in Relation to Cell Division, Celle Expansion and DNA Endoreduplication. *Ann. Bot.* **2005**, *95*, 439-447.

[62] Yoon, B.; Cho, E.; Baek, J.; Cho, I.; Woo, Y.; Choi, E. Comparison of Irrigation and Drainage Volumes, Growth and Fruit Yield under Different Automated Irrigation Methods in Tomato Rockwool Hydroponics. *Protected Horticulture and Plant Factory* **2020**, *29*, 1.

Appendix

A. Statistical analysis of the relationship between strain and resistance

Table A-1 is the result of a statistical analysis of Figure 4-3. According to Figure 4-3, liquid composite samples treated at 70℃ for 2 hours showed less variations in resistance between each sample compared to those treated at 70℃ for 4 hours. However, it was found that if we focus on individual samples, the samples treated at 70℃ for 4 hours has less mean standard deviations than those treated 70℃ for 2 hours. In other words, the samples with 70℃ for 4 hours showed more repeatable results than those with 70℃ for 2 hours in this experiment.

Table A-1. Statistical analysis of the relationship between strain and resistance based on the way of treatment of samples.

		Mean R^2		Mean standard deviation (kΩ)		Mean strain-resistance ratio (kΩ/mm)	
Sample condition	**Sample no.**	**Stretching**	**Releasing**	**Stretching**	**Releasing**	**Stretching**	**Releasing**
Non-heated	1	0.9943	0.9993	1.230	0.798	0.173	0.187
	2	0.9976	0.9966	1.077	1.600	0.224	0.213
	3	0.9969	0.9993	1.746	1.724	0.159	0.139
Heated at 70 ℃ for 2 hours	1	0.9995	0.9987	0.742	1.069	0.164	0.149
	2	0.9984	0.9973	0.903	1.651	0.178	0.162
	3	0.9988	0.9971	1.028	1.248	0.183	0.147
Heated at 70 ℃ for 4 hours	1	0.9923	0.9993	0.887	0.971	0.191	0.188
	2	0.9992	0.9988	0.622	0.743	0.164	0.157
	3	0.9962	0.9996	0.641	0.655	0.144	0.151

Table A-2 shows a statistical analysis of Figure 4-4. In this table, the sensitivity of the sensor is related to the mean strain-resistance. In other words, if resistance changes are greater at the unit displacement (1 mm), it can be said that the sensitivity is higher. Given this table, there is no remarkable difference in sensitivity among the samples stretched at different velocities. Therefore, it is

believed that no specific relationship between the sensitivity and the stretching velocity was confirmed.

Table A-2. Statistical analysis of the relationship between strain and resistance based on the stretching and releasing velocity of samples.

		Mean R^2		Mean standard deviation (kΩ)		Mean strain-resistance ratio (kΩ/mm)	
Sample condition	**Velocity (*μm/s*)**	**Stretching**	**Releasing**	**Stretching**	**Releasing**	**Stretching**	**Releasing**
Non-heated	20	0.9951	0.9991	0.396	0.324	0.128	0.125
	100	0.9988	0.9998	0.067	0.073	0.123	0.121
	200	0.9990	0.9999	0.141	0.213	0.124	0.123
Heated at 70 ℃ for 2 hours	20	0.9953	0.9963	0.567	0.632	0.107	0.105
	100	0.9983	1.0000	0.302	0.347	0.112	0.111
	200	0.9995	0.9996	0.626	0.414	0.109	0.111
Heated at 70 ℃ for 4 hours	20	0.9991	0.9996	0.384	0.271	0.104	0.105
	100	0.9995	0.9999	0.089	0.095	0.108	0.108
	200	0.9998	1.0000	0.082	0.155	0.109	0.107

B. Dendrometer requirements and specifications

Each fruit has different circumference ranges and growth rates. Table B-1 is the result of the investigation into these two factors of four fruits, which are apple, mandarin, passion fruit, tomato.

Table B-1. Requirements as a fruit dendrometer

	Apple	**Mandarin**	**Passion fruit**	**Tomato**
Circumference range (mm)	0 ~ 204 [60]	0 ~ 200 [31]	0 ~ 183 [31]	0 ~ 236 [61]
Growth rate (mm)	0.65 ~ 2.85 [12, 60]	0.64 ~ 1.29 [31]	0.01 ~ 0.14 [31]	0.47 ~ 12.56 [61]

To achieve the proper measurement of fruit growth, fruit dendrometers have to be designed and fabricated based on the properties of targeted fruits such as hardness, shape, circumference range, growth rate, size. Several types of

commercial dendrometers are available on the market as shown in Figure B-1.

Figure B-1. Commercial dendrometers and our dendrometer

It was found that most of the commercial fruit dendrometers are focused on measuring the diameter of fruits while our fruit dendrometer was designed to measure the circumference of fruits. The advantage of the circumference measurement system is that the users obtain more detailed information regarding fruit growth. Given that the diameter measurement system touches the two endpoints of fruits, it would be difficult to detect the growth of untouched areas. On the other hand, our fruit dendrometer can include the information about these areas by surrounding fruits as a circle.

Table B-2 is the summary of the specifications of the aforementioned commercial fruit dendrometers. One thing to be noted from this table is that compared to the commercial ones, our fruit dendrometer is light and can cover a large expansion range.

Table B-2. Dendrometer specifications

	DEX 70	**FI-MM**	**Type DF**	**Our dendrometer**
Circumference range (mm)	31 ~ 220	47 ~ 283	0 ~ 345	131 ~ 311
Expansion range (mm)	0 ~ 40	0 ~ 157 [62]	0 ~ 35	0 ~ 100

Length (mm)	102	132	-	237.5
Width (mm)	25.4	36	-	20.5
Height (mm)	51	140	-	4.0
Weight (g)	180	36	-	7.5

국문 초록

액상 중합체 및 금속염을 활용한 변형 센서의 제작 및 응용

서울대학교 대학원
기계항공공학부
이현재

다양한 분야에서 사용 목적에 따라 수많은 종류의 변형 센서들이 개발되어 왔다. 기계적 변형을 전기적 신호로 바꾸어 주는 본연의 기능에 기초하여 여러 물질들을 활용한 변형 센서 제작 방법이 소개되었다. 최근 스마트 농장이라는 이름으로 농업에 일련의 혁신이 일어나고 있는 가운데 고품질 작물을 얻기 위한 수요가 꾸준히 증가하고 있다. 식물 생장에 필수적인 정보를 획득하기 위한 방편 중 하나로 나무 줄기나 과실 크기를 측정하는 것이 중요해지고 있다. 이러한 목적의 도구들이 이미 보고된 바 있으나 기존 제품에 비하여 발전된 형태의 측수기(測樹器)에 대한 기대에 못 미친 것이 사실이다. 즉, 크기를 줄이고 작동 원리를 단순화하며 사용자 숙련도에 대한 의존성을 줄이는 동시에 가격적으로 경쟁력 있는 제품에 대한 필요성이 제기되어 왔다.

본 연구에서 액상 중합체 및 금속염(金屬鹽) 기반 신축성 변형 센서를 제안하였다. 신체 등의 즉각적인 움직임을 감지하기 위한 착용형(着用型) 센서로 쓰이는 종래의 변형 센서들에 비하여, 새로이 개발된 센서에는

전도성(傳導性) 액체로 질산은과 폴리에틸렌글리콜(PEG)의 혼합물이 적용되었다. 이 액상 중합체를 통하여 높은 점도와 화학적 안정성을 도모하면서 질산은을 이용하여 전해질을 전도성 액체에 공급할 수 있다. 신축성 변형 센서의 골격은 탄성 중합체인 폴리디메틸실록산(PDMS)과 에코플렉스(Ecoflex)로 만들었다. 반복적인 실험을 거쳐 최적의 배합 비율(PDMS 20:80 Ecoflex)을 찾음으로써 효과적인 과실 생장 관찰에 필요한 변수인 변형, 응력(應力), 마찰의 적절한 타협점을 알아낼 수 있었다. 신축성 변형 센서의 성능 분석 결과, 변형과 저항 사이에 높은 선형성을 보이는 것이 확인되었다. 과실 생장 관찰을 통하여 2주 동안 약 1.7 ~ 3.9 kΩ/mm의 범위 내에서 신축성 변형 센서가 안정적으로 작동하는 것을 증명하였다. 과실 생장 측정을 위한 대안적인 도구로서, 이번에 개발된 조정 가능한 밴드형 센서는 제작 공정이 단순하고 신뢰성 있는 측정이 가능하며 장기간 평가에 적합하다는 면에서 우수한 잠재성을 가지고 있다고 말할 수 있을 것이다.

질산은과 PEG의 조합을 이용하여 더듬이 형태의 생체모방 촉각 센서도 선보였다. 이 전도성 액체는 곤충의 더듬이 내에서 림프로 이루어진 부분(lymph space)을, 금속 전선은 관 모양의 구조물(tubular body)을 구현하는 데 활용되었다. 특히 이 관 모양의 구조물은 곤충의 촉각에서 기계적 변형을 전기적 신호로 바꾸어 중추 신경계로 전달하는 역할을 한다. 이 생체모방 촉각 센서는 어두운 공간에 노출된 시각 센서의 오작동에서 비롯되는 문제를 보완하기 위하여 고안되었다. 3D 프린터로 제작된 요철이 있는 벽면을 가지고 스캔 실험을 진행한 결과

촉각 센서가 굽히는 각도와 저항 사이에서 반복적이면서 선형적인 관계가 형성된다는 것을 증명하였다. 아울러 금속 전선이 전도성 액체에 놓이는 위치에 따라 촉각 센서의 저항이 결정된다는 사실도 밝혔다. 그리고 촉각 센서와 벽면 사이 거리가 고정되어 있다는 가정하에 스캔 실험을 실시한 결과 벽면의 요철을 높은 정확도로 재구성할 만큼 신뢰성 있는 값을 제공한다는 것을 알 수 있었다. 이 더듬이 형태의 생체모방 촉각 센서는 기존의 촉각 센서와 비교하였을 때 새로운 물질이 적용되었고 상대적으로 단순한 제작 공정을 통하여 제작되었다. 기존 촉각 센서와 다른 작동 원리에 대한 이해를 높이는 동시에 센서가 굽히는 각도와 저항 사이의 높은 반복성을 확립함으로써 후속 연구를 통하여 동일 센서를 활용한 3차원 이미지 재구성에 대한 가능성도 엿볼 수 있었다.

주요어 : 액상 중합체, 폴리에틸렌글리콜, 질산은, 측수기, 과실 생장, 촉각 센서

학 번 : 2015-30163